Department of Physics and Astronomy
Heidelberg University

Bachelor Thesis in Physics
submitted by

Ruben Benjamin Henninger

born in Bad Mergentheim (Germany)

2022

Production, transfer and re-trapping of highly charged Ar^{14+} from an electron beam ion trap into a superconducting cryogenic Paul trap

This Bachelor Thesis has been carried out by Ruben Benjamin Henninger at the
Max-Planck-Institut für Kernphysik in Heidelberg
under the supervision of
Prof. Dr. José Ramón Crespo López-Urrutia

Abstract:
High precision spectroscopy of highly charged ions demands ultra cold and stable environments, a prerequisite uncommon for their location of production. To evade this difficulty, the CryPTEx-II experiment spatially separates the ion production from storage by trapping these inside a cryogenic superconducting Paul trap. During this thesis, argon ions were produced inside an electron beam ion trap and guided through a beamline towards the Paul trap. The different charge states that made up the ion beam were identified by their time of flight and a single charge state, Ar^{14+}, was selected. These selected ions were decelerated and bunched inside a pulsed drift tube and injected into a Paul trap biased to an elevated potential. Electrodes acting as mirrors for charged particles reflected the ion bunch multiple times inside the trap. Meanwhile, a Coulomb crystal of Be^{+} ions cooled the reflected ions sympathetically. Finally, Ar^{14+} ions were stopped inside the crystal, demonstrating the successful transfer of a highly charged ion into an ultra cold environment suitable for precision spectroscopy.

Zusammenfassung:
Die Hochpräzisionsspektroskopie hochgeladener Ionen erfordert eine extrem kalte und stabile Umgebung, eine Voraussetzung, die für den Ort ihrer Erzeugung ungewöhnlich ist. Um diese Schwierigkeit zu umgehen, trennt das CryPTEx- II-Experiment die Ionenproduktion räumlich von der Speicherung, indem es diese in einer kryogenen supraleitenden Paul-Falle einfängt. Im Rahmen dieser Arbeit werden Argon-Ionen in einer Elektronenstrahl-Ionenfalle erzeugt und durch ein Strahlrohr zur Paul-Falle geleitet. Die verschiedenen Ladungszustände, aus denen der Ionenstrahl besteht, wurden anhand ihrer Flugzeit identifiziert und ein einziger Ladungszustand, Ar^{14+}, ausgewählt. Die ausgewählten Ionen wurden in einer gepulsten Driftröhre abgebremst und gebündelt und in eine auf ein erhöhtes Potenzial gesetzte Paul-Falle injiziert. Elektroden, die als Spiegel für geladene Teilchen fungierten, reflektierten das Ionenbündel mehrfach innerhalb der Falle. In der Zwischenzeit kühlte ein Coulomb-Kristall aus Be^{+}-Ionen die reflektierten Ionen sympathetisch ab. Schließlich wurden die Ar^{14+}-Ionen im Inneren des Kristalls gestoppt, was den erfolgreichen Transfer eines hochgeladenen Ions in eine ultrakalte, für die Präzisionsspektroskopie geeignete Umgebung demonstrierte.

Contents

1 Introduction

Today, modern physic can describe most of the nature with only four fundamental interactions, three of which are described in the so-called standard model of particle physics [1]. However, we know that the standard model has difficulties explaining certain phenomena, such as the asymmetry between matter and antimatter or the accelerated expansion of the universe [2, 3]. The latter could be explained by the existence of a so-called dark energy. Therefore, physicists around the world try to expand our knowledge by searching for unknown particles, forces or merely hints of new physics like dark energy.

This search is done at multiple frontiers, using different approaches. Large facilities like CERN or Fermilab carry out experiments at extremely high energies, searching for new particles, resulting, e.g., in the discovery of the Higgs boson. On the other side of the spectrum, experiments operating at low energy and high precision can also probe our theories for the search for new physics. One example is the measurement of parity nonconservation in atomic transitions to test the electroweak unification [4].

With such precision experiments, a whole range of tests can be done, for example, to investigate whether the fundamental constants are in fact truly constant. Some theories of physics beyond the standard model predict variation in, e.g., the fine structure constant $\alpha = e^2/\hbar c$ [5]. Evidence for deviations was already observed in the spectra of quasars [6]. A proposed shift of α due to increased gravitation is proposed to lie in the order of $10^{-19}\mathrm{yr}^{-1}$ on earth [6].

Since the fine structure constant is the coupling strength of the electromagnetic force, a test on based on spectroscopy would be a natural choice. The method of observing light for its spectral information, pioneered by Kirchhoff and Bunsen [7], probes the internal configuration of atomic or ionic systems. This also found use in metrology, offering a new definition of the second with the microwave spectroscopy of caesium [8]. A more recent approach to time or frequency metrology is the use of optical atomic clocks, operating in the visible spectrum of electromagnetic radiation. These often use experimental setups like optical lattices or ion traps, which feature the ability to do spectroscopy on well-defined systems [9, 10].

However, the sensitivity of a transition to variations of α is dependent on the relativistic contribution of the involved energy levels [11]. Therefore, highly charge ions (HCIs) offer a higher sensitivity compared to neutral atoms or singly charged ions, due to their increased coupling between the nuclei and their residual electrons. This characteristic gave rise to the interest in optical atomic clocks based on transitions in HCIs [12]. Even though this advantage and other features of HCIs, such as robustness against external fields, seems promising, the production and handling of HCIs is subject to certain difficulties. In nature, HCIs only occur in extreme places, like the sun's corona [13]. Highly charged ions are produced with high energies due to their subsequently increasing ionization energy,

resulting in extreme temperatures. This renders high precision spectroscopy impossible due to Doppler broadening of spectral lines [14].

The cryogenic Paul trap experiment II (CryPTEx-II) aims to overcome this problem by sympathetic cooling of retrapped HCIs. Its predecessor, CryPTEx, trapped HCIs inside a cryogenic Paul trap for the first time, demonstrating a process enabling high precision spectroscopy of HCIs [15]. Both experiments and a "sister setup" at the physikalisch-technische Bundesanstalt (PTB) are based on the same principle. HCIs are produced inside an electron beam ion trap, a device capable of producing high charge states through electron impact ionization. The ions are then transferred into a Paul trap, where they are stopped inside a laser cooled Be^+ ion ensemble. This offers the possibility of single ion spectroscopy by methods like quantum logic spectroscopy [16]. The setup at the PTB operates already as an atomic clock and showed promising results [17]. CryPTEx-II is intended to further advance the ongoing experiments. Therefore, the ions are trapped inside a superconducting cryogenic Paul trap [18]. In combination with a newly build XUV frequency comb [19], this setup will allow probing HCIs for their internal states, in the end representing an atomic clock.

Every clock needs its oscillator and in this work, the crucial process of retrapping an HCI is implemented in our setup, starting with the production of HCIs inside an EBIT. These get transferred to the Paul trap setup via a beamline, providing a selection method to differentiate the individual charge states of the produced HCIs. After selection, the ion beam will be decelerated and finally injected into the Paul trap. Through reflection between two mirror electrodes at both ends of the radio frequency field, the ions will be reflected through a Be^+ Coulomb crystal until sympathetic cooling reduced the kinetic energy so far that the HCIs will be caught inside the Paul trap centre.

2 Theoretical background

In this chapter, the theoretical background for the following measurements and experiments is introduced. Section 2.1 gives an overview of the electron beam ion trap (EBIT) and explains how highly charged ions are produced. Subsequently, Section 2.2 describes how electric fields can be used to transport and influence charged particles. Afterwards, Section 2.3 covers the ideal Paul trap and how it is used to store charged particles, Section 2.4 explains how lasers can be used to cool atomic or ionic systems and lastly section 2.5 explains the concept of retrapping an HCI.

2.1 Electron beam ion trap

Electron beam ion traps can be used to produce and store highly charged ions (HCIs). The EBIT was developed at the Lawrence Livermore National Laboratory by Levine et al. [20]. EBITs trap ions with a magnetically compressed electron beam and a positive electric potential provided by trap electrodes. At first, EBITs were used to study HCI interactions and spectra, as well as plasma behaviour without the need to build large accelerators or plasma experiments like Tokamaks, but EBITs can also be used as a source for HCIs to provide them for other experiments or applications [20].

In this work, a so-called Heidelberg Compact electron beam ion trap (HC-EBIT) was used to produce highly charged argon ions [21]. In this section, the working principle of an EBIT and the important electronic processes are discussed to see how the high charge states are produced and how charge states evolve over time.

2.1.1 Working principle of an electron beam ion trap

In Figure 2.1, the schematic depiction of an EBIT is shown, including the relevant potentials, particles and magnetic fields. According to Earnshaw's theorem [22], a charged particle cannot be trapped solely by electric or magnetic static potentials in a source free space. Thus, an EBIT uses two different electric potentials, only one of which is source free, evading the restrictions of Earnshaw's theorem. For particle confinement in the direction of the electron beam, the so-called axial direction, the trap uses electrostatic fields supplied by cylindrical trap electrodes, so-called drift tubes. To restrain the charged particles in the remaining two spatial dimensions, the so-called radial direction, the EBIT makes use of the space charge of the compressed electron beam. Thus, the potential landscape of an EBIT has a potential well in all three spatial dimensions.

The main components needed to produce an electron beam are an electron gun followed by an inhomogeneous magnetic field and a collector electrode. To generate a stable

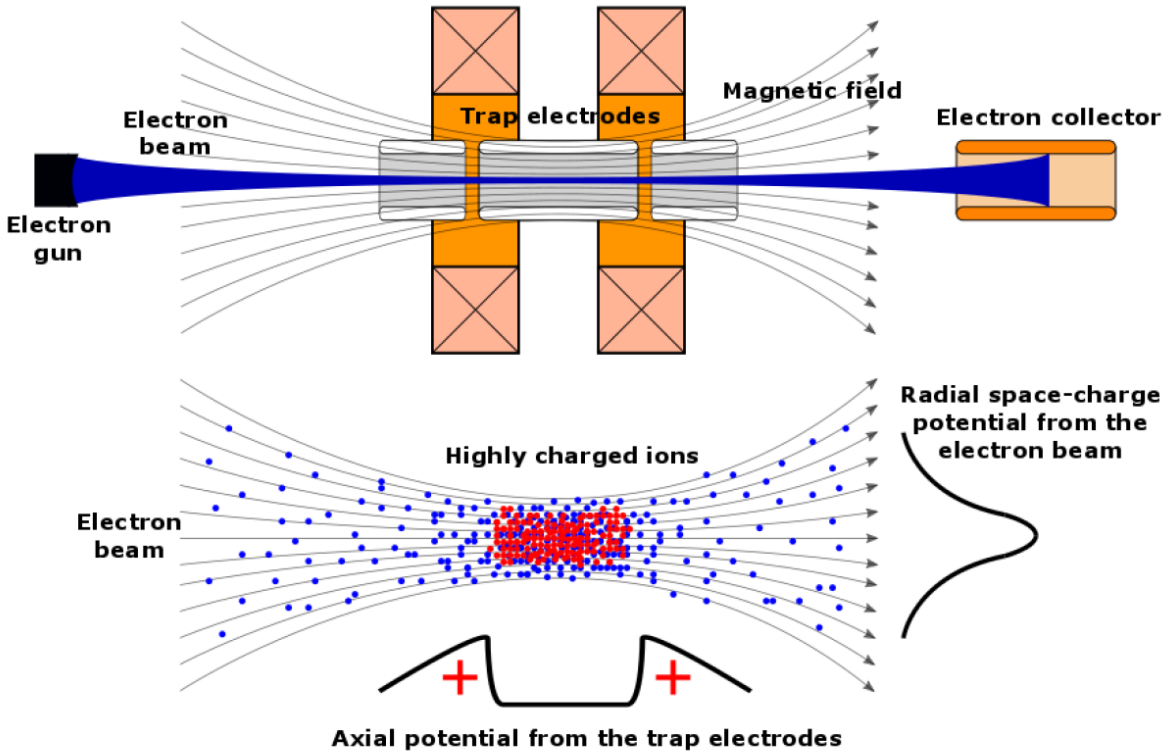

Figure 2.1: Simplified depiction of the fundamental parts and potentials of an EBIT. Top: Schematic of the essential parts of an EBIT with trap electrodes (white) for axial confinement, the electron beam (blue) is emitted by the heated cathode of the electron gun, compressed by a magnetic field (orange magnets) and neutralized inside the collector. Bottom: Ions (red) are axially confined by the potential provided by positively charged drift tubes and radially confined by the space charge of the electrons (blue). Taken from [23]

.

electron beam, electrons are thermionically emitted by a heated cathode and accelerated by a voltage bias between the cathode and an anode directly in front of the cathode. The magnetic field compresses the diameter of the electron beam to focus it in the trap centre in between the drift tubes. After passing the drift tubes, the electron beam expands due to the lack of the magnetic field, is decelerated by an electric field, and dumped on the collector electrode. The drift tubes are six electrodes, three of which allow control over beam properties, while the residual three electrodes act as trapping electrode. These will be set to a positive voltage to produce a potential minimum in which the HCIs can be trapped. Therefore, the outer drift tubes are set to higher voltages than the central one.

All processes, including production and storage of HCIs happen inside this central drift tube. To produce and store ions, a neutral gas jet is injected into this region. By colliding with the electron beam, the neutral atoms become ionized via electron impact ionization (EII) and start to be affected by the space charge and attracted towards the

trapping potentials minima. This leads to further ionization by subsequent EII until the energy of the electrons no longer exceeds the ionization energy of the least bound electron.

2.1.2 Electronic processes

Inside the trap centre, a variety of different processes and interactions happen between the ions, the incoming neutral atoms, residual gas and the electron beam. An overview of most processes is given in [24]. In the following section, only the main processes important for the charge state distribution and evolution will be discussed. This description follows [25] and [26] in their explanation of the processes inside an EBIT.

Electron impact ionization

If the energy E_e of an electron e^- exceeds the ionization energy I_p of an atom or ion A, it can ionize A by impact ionization. Hereby, the charge state q will be increased by one. Assuming a typical cross-section of $10^{16}\mathrm{cm}^2$ for EII and typical EBIT operation conditions for the electron beam current density of $10^{22} e\,\mathrm{s}^{-1}\,\mathrm{cm}^{-2}$ leads to an initial ionization rate in the MHz range [26]. As we will see, this makes EII the dominant process occurring in an EBIT. Because of the high energy of the electron beam, the atoms do not only get ionized into the first charge state, but subsequently reach higher charge states by continuous electron bombardment until the ionization energy overcomes the electron beam energy.

$$\mathrm{A}^{q+} + \mathrm{e}^-(E_\mathrm{e}) \longrightarrow \mathrm{A}^{(q+1)+} + \mathrm{e}^-(E_1) + \mathrm{e}^-(E_2). \tag{2.1}$$

Here E_1 and E_2 denotes the energy of the two out coming electrons, for which $E_e - I_p = E_1 + E_2$ holds true. A semiempiric estimation for the cross-section σ_EII of this interaction is given by [27] with

$$\sigma_\mathrm{EII} = 4.49 \times 10^{-14}\mathrm{cm}^2\,\mathrm{eV}^2\,\frac{N}{I_p^2}\,\frac{\ln(u+1)}{u+1}, \tag{2.2}$$

where $u = E_\mathrm{e}/I_p - 1$ and N is the number of equivalent electrons in the same shell.

Radiative recombination

Ions can also absorb a free electron under emission of a photon. This process of radiative recombination (RR) lowers the charge state by one.

$$\mathrm{A}^{q+} + \mathrm{e}^- \longrightarrow \mathrm{A}^{(q-1)+} + \hbar\omega_\mathrm{RR}. \tag{2.3}$$

The energy of the photon $E_\gamma = \hbar\omega_\mathrm{RR} = E_\mathrm{e} + I_p$ is given by the conservation of energy as the energy of the electron E_e and the binding energy of the ion in the final state I_p. The

cross-section σ_{RR} can be estimated by a semi-empirical formula from [28] as

$$\sigma_{\mathrm{RR}} = \frac{8\pi\alpha\lambda_C^2\chi}{3\sqrt{3}} \ln\left(1 + \frac{\chi}{2(n_0)_{\mathrm{eff}}^2}\right) \quad \text{with} \quad \chi = 2Z_{\mathrm{eff}}^2 \frac{I_{\mathrm{H}}}{E_e}, \tag{2.4}$$

the fine structure constant α, the electron Compton wavelength $\lambda_c = 3.861 \times 10^{-11}\,\mathrm{cm}$ and I_{H} the ionization potential of the hydrogen atom. The parameters $Z_{\mathrm{eff}} = 0.5(Z+q)$ and $(n_0)_{\mathrm{eff}} = n_0 + (1 - W_{n_0}) - 0.3$ depend on the charge state q, the nuclear charge Z, the valence shell number n_0 and the ratio W_{n_0} between the number of occupied states and the total number of states [25].

Charge exchange

Another process, taken into account here, is the interaction between the ions and a neutral atom B. These could be residual gas left inside the vacuum system or unionized atoms from the injection system. By collision, B gets ionized and A gains one electron, thereby lowering the charge state.

$$\mathrm{A}^{q+} + \mathrm{B} \longrightarrow \mathrm{A}^{q-1} + \mathrm{B}^{+} + \hbar\omega_{\mathrm{CX}}. \tag{2.5}$$

Such low collision energy interactions have a cross-section

$$\sigma_{\mathrm{CX}} = 1.4310 \times 10^{-12} q^{1.17} I_p^{-2.76}, \tag{2.6}$$

estimated in [29], where q is the charge state of the ion and I_p is the ionization energy of the neutral atom.

2.1.3 Charge-state distribution

With the processes described above, one can calculate the individual density rates R at which ions are produced and increase or decrease their charge state.

$$\begin{aligned} R_{q\to q+1}^{\mathrm{EII}} &= \frac{J_e}{e} n_q\, \sigma_{\mathrm{EII}}\, f(r_e, r_i), \\ R_{q\to q-1}^{\mathrm{RR}} &= \frac{J_e}{e} n_q\, \sigma_{\mathrm{RR}}\, f(r_e, r_i), \\ R_{q\to q-1}^{\mathrm{CX}} &= n_0(p_{\mathrm{in}})\, n_q \sigma_{\mathrm{CX}} \bar{v}_q, \end{aligned} \tag{2.7}$$

Here, J_e is the electron beam current density, n_q the ion density, $f(r_e, r_i)$ an overlap factor between the beam r_e and the ion cloud r_i, n_0 the neutral gas density, which depends on the injection pressure p_{in}, and v_q the velocity of the ions according to the Maxwell-Boltzmann distribution.

For the total rate equation, we also have to account for the escape of ions from the trap. This depends on the depth of the trapping potential, and therefore differs for axial or radial escape.

$$R_q^{\mathrm{esc}} = -n_q \nu_q \left(\frac{e^{-\omega_q}}{\omega_q} - \sqrt{w_q}\,[\mathrm{erf}(\omega_q) - 1]\right) \quad \text{, with} \quad \omega_q = \frac{eZ_q V_\omega}{k_B T_q}, \tag{2.8}$$

with the total Coulomb collision rate ν_q, the Boltzmann factor k_B, the temperature T_q and the depth of the potential well V_ω, either in axial direction V_{ax}, or radial direction V_{rad}. Taking now all these rates into account, the overall rate R_q^{tot}, and hence also the single charge states q can be written down as

$$\begin{aligned} R_i^{\mathrm{tot}} &= \frac{dn_i^{\mathrm{tot}}}{dt} \\ &= R_{q-1\to q}^{\mathrm{EII}} - R_{q\to q+1}^{\mathrm{EII}} + R_{q+1\to q}^{\mathrm{RR}} - R_{q\to q-1}^{\mathrm{RR}} + R_{q+1\to q}^{\mathrm{CX}} - R_{q\to q-1}^{\mathrm{CX}} \\ &\quad - R_q^{\mathrm{radesc}} - R_q^{\mathrm{axesc}}. \end{aligned} \tag{2.9}$$

This can be numerically calculated, seen for example in [25] or [30] to obtain the evolution of charge states depending on the number of injected atoms or breeding time.

2.1.4 Extraction

In this work, the EBIT is used as a source of HCIs. Thus, a way of extracting the ions from the trap is needed. By raising the potential of the innermost trap electrode above the potential of the outer electrodes, one can kick out the ions axially in one pulse. This extraction usually takes place with a certain frequency, allowing a similar charge state distribution every extraction. The emitted ion bunch is characterized by two main properties that will be described in the following.

Beam velocity

The energy E_{ion} of the HCIs mainly depend on the acceleration caused by the higher potential of the inner trap electrode, as well as the thermal energy E_T gained inside the EBIT and the potential from the space charge ϕ_{SC} [30]. Therefore, an ion with charge state q has the energy

$$E_{\mathrm{ion}} = qe(\kappa\phi_{\mathrm{kick}} + \phi_{\mathrm{SC}}) + E_T, \tag{2.10}$$

with a correction factor κ accounting for ions that leave the trap before reaching ϕ_{kick}, but already high enough to leave the axial confinement.

For further calculations, we can neglect the effect of the space charge potential and the thermal energy of the ions. The former effect would lower the ion's energy and the latter one is negligible when investigating the ion energy, but contributes to the energy spread ΔE_{ion} of the ion bunch. κ can be set to $\kappa \approx 1$, because of the low kick voltage used during the experiments [30]. This leaves us

$$E_{\mathrm{ion}} \approx qe\phi_{\mathrm{kick}} \quad \text{, with} \quad \Delta E_{\mathrm{ion}} \approx \Delta E_T. \tag{2.11}$$

The energy of the ion is translated into kinetic energy while leaving the trap, hence the velocity v_{ion} can be estimated as

$$v_{\mathrm{ion}} = \sqrt{\frac{2E_{\mathrm{ion}}}{m}} = \sqrt{\frac{2qe\phi_{\mathrm{kick}}}{m}}. \tag{2.12}$$

Beam divergence

Due to the temperature T inside the EBIT, the emitted ions not only obtain the above described mean velocity along the beam axis, but also statistically distributed velocities components in all directions. Therefore, the beam also possesses a radial velocity distribution. These components will lead to a broadening of the beam described by the emittance ϵ of the beam, given by

$$\epsilon = \pi r r', \tag{2.13}$$

where r is the waist diameter of the beam and r' is the divergence angle of the beam. The emittance of an EBIT is given by [31]:

$$\epsilon = \pi R_{80} \sqrt{\frac{T}{qe\phi_{\text{kick}}}} = \frac{\pi R_{80}\sqrt{2T}}{\sqrt{m}v_{\text{ion}}}, \tag{2.14}$$

with R_{80}, the beam diameter containing 80% of all ions. One should note that this radius depends on the distribution describing the ions' velocity. Thus, we see that the due to the temperature distribution of the ions inside the beam, repetitive refocusing of the beam along its further path is necessary. Additionally, the space charge of the ions themselves leads to a broadening of the ion beam. This is further discussed in [32]. Besides, we see that the emittance also depends on the ion velocity. The beam will diverge more for small axial velocities.

2.2 Ion optics

As shown in the last chapter, the ion beam leaving the trap needs to be refocused to compensate for the emittance of the beam. To gain control over charged particles, one can use interactions with other charged surfaces or particles to deflect, accelerate, or steer the beam. Because of strong parallels between optical components affecting a laser beam and electronic components affecting a charged particle beam, these electrical components are often referred to by the name of their optical counterpart. Steering, refocusing and deceleration take place inside a beamline. It contains several electrostatic elements for beam manipulation, but also a dynamical system used to decelerate the ions. This is described in section 2.2.3.

2.2.1 Electrostatic optics

For the purpose of beam focusing or steering, the beam is interacting with different potentials applied along the beamline. As stated above, the electrodes supplying these potentials are ion optical elements, or electron optical elements, referring to their first use in electron microscopes [33]. The theoretical description of the electrodes specified below and the effect of the electric fields follows [34]. A deeper analysis of electrostatic components and their influence on charged particle beams is given in [35].

Trajectories in electromagnetic fields

To describe the full motion of an ion in the presence of electromagnetic fields, we need to derive the equation of motion for a charged particle with mass m, charge state q and velocity vector $\vec{v}$ in the presence of an electric potential ϕ and a magnetic potential $\vec{A}$, following the description in [32]. These can be derived by the Lagrange formalism from the Lagrangian L of said particle, which is given by [36]

$$L = \frac{-mc^2}{\gamma} - qe\phi + qe\vec{A}\vec{v}. \tag{2.15}$$

Here c is the speed of light, e the elementary charge and γ is the Lorentz factor given by

$$\gamma = \frac{1}{1-\beta^2} \quad \text{with} \quad \beta = \frac{v}{c}. \tag{2.16}$$

This Lagrangian obeys the Euler-Lagrange equation:

$$\frac{\mathrm{d}}{\mathrm{d}t}\frac{\partial L}{\partial \dot{s}_i} - \frac{\partial L}{\partial s_i} = 0, \tag{2.17}$$

with the generalized coordinates $\vec{s}$. Here and in the following, subscript i denotes the component of the mentioned vectors. Now we want to use the spatial coordinate $\vec{r}$ and its time derivative, the velocity $\vec{v}$. Therefore, we get

$$\begin{aligned} \frac{\mathrm{d}}{\mathrm{d}t}\frac{\partial L}{\partial v_i} &= \frac{\mathrm{d}}{\mathrm{d}t}\left(\gamma m v_i + qeA_i\right) = \frac{\mathrm{d}\vec{p_i}}{dt} + qe\,\frac{\mathrm{d}A_i}{dt}, \\ \frac{\partial L}{\partial r_i} &= \nabla_i L = -qe\nabla_i\phi + qe\nabla_i\left(A_i v_i\right). \end{aligned} \tag{2.18}$$

with the relativistic momentum $\vec{p} = \gamma m\vec{v}$. By transforming the second equation using Grassmann's identity and inserting everything in eq. (2.17), we obtain an equation for the momentum of the particle given by

$$\frac{d\vec{p}}{dt} = qe\left(-\nabla\phi - \frac{\partial\vec{A}}{\partial t}\right) + qe\left(\vec{v}\times\left(\nabla\times\vec{A}\right)\right). \tag{2.19}$$

This equation describes the whole trajectory in arbitrary potentials. This equation can be rewritten in terms of the magnetic field $\vec{B}$ and the electrostatic fields $\vec{E}$, using

$$\vec{E} = -\nabla\phi - \frac{\partial\vec{A}}{\partial t} \quad \text{and} \quad \vec{B} = \nabla\times\vec{A}. \tag{2.20}$$

With this, the equation of motion based on the Lorentz force $\vec{F_L}$ is derived:

$$\frac{d\vec{p}}{dt} = qe\left(\vec{E} + \vec{v}\times\vec{B}\right) =: \vec{F_L}. \tag{2.21}$$

This equation of motion also holds for relativistic particles. However, the velocities reached in this work do not extend into relativistic regions. For an Ar^{14+} ion being extracted from an EBIT with a kick potential around 1 kV,we obtain with eq. (2.12) a velocity of:

$$v_{\text{ion}} = \sqrt{\frac{2 \cdot 14 \cdot e \cdot 1000\,\text{V}}{40 \cdot 931.5\,\text{MeV}\,c^{-2}}} \approx 0.000\,725\,9\,c = 217.6\,\text{km}\,\text{s}^{-1}. \tag{2.22}$$

This allows for a non-relativistic treatment of all processes in this section. Furthermore, all relevant elements used in the setup employed for this thesis only feature electrostatic systems without any magnetic fields. Hence, we also neglect the magnetic part of the Lorentz force and the electric field and get

$$\vec{F} = qe\vec{E} = qe\vec{\nabla}\phi. \tag{2.23}$$

In a first step, this equation will be solved for a constant force $\vec{F}$ generated by an electrostatic potential [30]. By integration $\ddot{\vec{r}} = \vec{a_0} = const.$ of the equation above, we obtain the trajectory

$$\vec{r} = \frac{\vec{a_0}}{2}t^2 + \vec{v_0}t + \vec{r_0}. \tag{2.24}$$

with the initial values $\vec{r_0}$, $\vec{v_0}$, and $\vec{a_0}$, of particle position, velocity and acceleration, respectively. Now we insert the initial values for an ion beam leaving an EBIT, described in section 2.1. Therefore, we set $\vec{v_0} = \vec{v_{\text{ion}}}$, $\vec{r_0} = 0$ and $\vec{a_0} = 0$. Given the electrostatic force, this can be rewritten with $\vec{a} = \vec{F}/m$ and a newly defined time parameter $\tau = \sqrt{qe/m}t$, to form a new equation of motion.

$$\vec{r}(\tau) = \frac{\nabla\phi}{2}\tau^2 + \sqrt{2\phi_{\text{kick}}}\tau. \tag{2.25}$$

We see that in electrostatic potentials, the trajectory should not depend on the charge state of the ion. This does not hold true for their time of flight. Two ions A and B with charge state q_{A} and q_{B}, respectively, arrive at a certain position $\vec{r}$, e.g. a detector in our experiment, at the same value of τ.

$$\tau_{\text{A}} = \tau_{\text{B}} \iff \sqrt{\frac{q_{\text{A}}e}{m_{\text{A}}}}t_A = \sqrt{\frac{q_{\text{B}}e}{m_{\text{B}}}}t_{\text{B}}, \tag{2.26}$$

which leads to

$$t_{\text{A}} = \sqrt{\frac{q_{\text{B}}m_{\text{A}}}{q_{\text{A}}m_B}}t_{\text{B}}. \tag{2.27}$$

Neglecting the small mass difference between ions of single element in different charge states, which is small due to the small electron mass, we can calculate the time of flight for ion A depending on the singly charged ion C of the same mass to be

$$t_A = \frac{t_{\text{C}}}{\sqrt{q_{\text{A}}}}. \tag{2.28}$$

From eq. (2.21) alone, the whole trajectory of the individual ions flying inside the beam could be calculated. For some field configurations, the trajectory of a single charged particle can be solved analytically. However, for an ion beam consisting of many particles travelling through a complex potential landscape, numerical simulations are used. To illustrate the function of basic electrostatic components, the trajectories of a single charged particle for two simple field configurations are analytically derived in the following.

Unitary field

Two cases for the orientation of electrostatic fields are discussed in the following, which can be used to reconstruct all potentials along the beamline. First a potential change along the flight path of a charged particle and then a potential change perpendicular to the path will be described. The description follows [34].

Parallel electric field First, a potential change along the flight path of a particle with mass m and charge state q is discussed. Therefore, a two-dimensional coordinate set is used with the directions z and r. The particle encounters an acceleration $m\ddot{z} = qeE$ in z direction through the E-field, by the potential changing from V_1 to V_2 ($V_1 < V_2$) over the length L. It enters the potential on an angle α_1 with respect to the z axis. It only possesses kinetic energy qeV_1 in flight direction. In this case, we can solve the equation eq. (2.21) by integration with the given start values and obtain the motion in the z-r plain as a function of time:

$$\dot{z} = \frac{qeE}{m}t + v_1 \cos\alpha_1, \qquad z = \frac{qeE}{2m}\,t^2 + v_1 \cos\alpha_1 t, \tag{2.29}$$

$$\dot{r} = \dot{r_1} = v_1 \sin\alpha_1, \qquad r = v_1 \sin\alpha_1 t. \tag{2.30}$$

Here v_1 is the velocity of the incoming particle originating from the kinetic energy mentioned above with $v_1 = \sqrt{2eqV_1/m}$. In these equations, the time t can be eliminated by solving eq. (2.29) for t with respect to z to obtain a trajectory $r(z)$:

$$t = \frac{mv_1}{qeE}\left(\sqrt{\cos^2\alpha_1 + \frac{E}{V_1}z} - \cos\alpha_1\right), \tag{2.31}$$

$$r(z) = \frac{2V_1}{E}\sin\alpha_1\left(\sqrt{\frac{E}{V_1}z + \cos^2\alpha_1} - \cos\alpha_1\right). \tag{2.32}$$

From this trajectory, we can now calculate the distance r_2 from the z axis at $z = L$, where the particle leaves the potential change. Therefore, we rewrite from the definition of the E-field

$$\frac{E}{V_1} = \frac{1}{L}\left(\frac{V_2}{V_1} - 1\right). \tag{2.33}$$

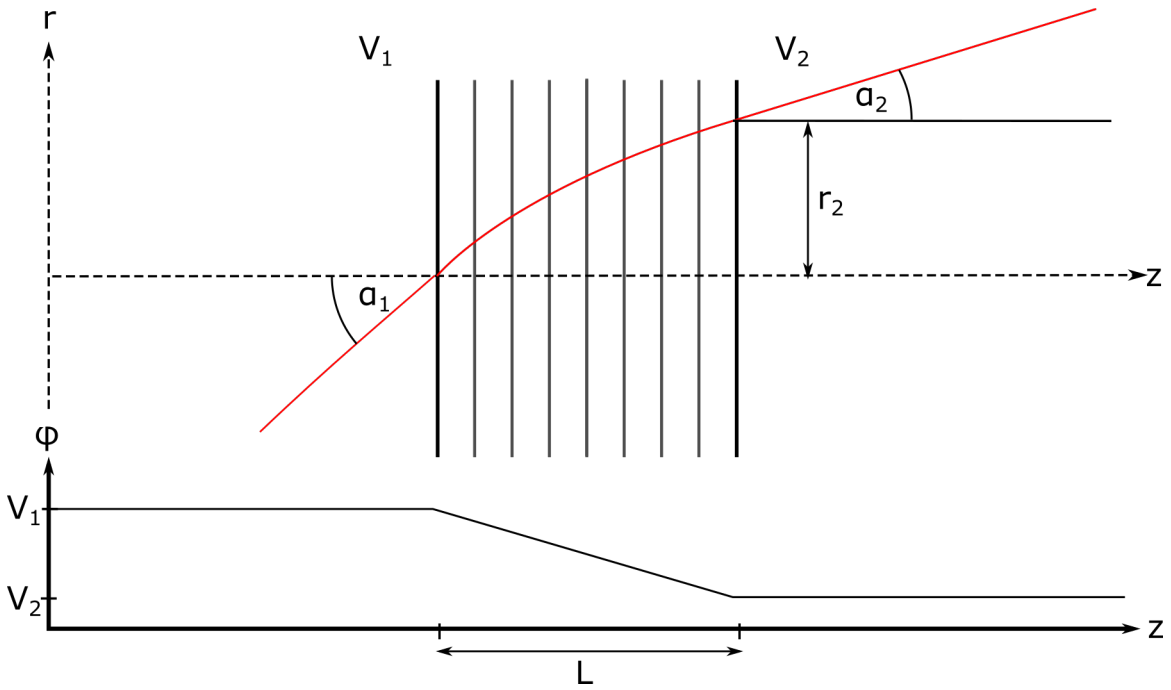

Figure 2.2: Trajectory (red) of a charged particle in parallel electric field. The potential along the flight path declines V_1 to V_2, indicated by thin black equipotential lines. Below, the potential along the z axis is shown. Adapted from [34]

Using this we obtain r_2 as

$$r_2 = \frac{2L \sin \alpha_1}{\frac{V_2}{V_1} - 1} \left(\sqrt{\frac{V_2}{V_1} - \sin^2 \alpha_1} - \cos \alpha_1 \right) \tag{2.34}$$

To obtain the slope of r_2 with respect to z we use eq. (2.32), solving for r with respect to z and set $z = L$. This yields:

$$r_2' = \sin \alpha_1 \left(\frac{V_2}{V_1} - \sin^2 \alpha_1 \right)^{-\frac{1}{2}} \tag{2.35}$$

From this we can now derive a "refractive index" for charged particles. For this, we use the geometrical interpretation of r_2' by rewriting it to

$$r_2' = \tan \alpha_2 = \frac{\sin \alpha_2}{\sqrt{1 - \sin^2 \alpha_2}} \tag{2.36}$$

and putting it into eq. (2.35) we get

$$\frac{\sin \alpha_2}{\sin \alpha_1} = \frac{\sqrt{V_1}}{\sqrt{V_2}} \tag{2.37}$$

This equation is very similar to its optical counterpart: Snell's law of refraction. Here $\sqrt{V_1}$ and $\sqrt{V_2}$ act as the effective refractive index of their potentials V_1 and V_2. However,

it is only fully equivalent for an infinitesimally small L and therefore no deviation r_2 to the z axis.

All calculations above can also be done with $V_1 < V_2$, leading to a deceleration of the particle. This scenario features a special solution, when the term under the square root in eq. (2.35) becomes negative. This is equivalent to the reflection of the particle and will lead to a parabolic trajectory of the particle. The first few steps of the calculation are the same until we solve eq. (2.30) for t and insert it into eq. (2.29) and consequently obtain

$$z = \frac{E}{4V_1}\frac{r^2}{\sin\alpha_1} + \frac{r}{\tan\alpha_1}. \tag{2.38}$$

From this we can also calculate the turning point inside the potential and the deviation in r with

$$r_m = -2\frac{V_1}{E}\sin\alpha_1\cos\alpha_1 \tag{2.39}$$

$$z_{\max} = \frac{E}{4V_1}\frac{r_m^2}{\sin^2\alpha_1} + \frac{r_m}{\tan\alpha_1} = \frac{V_1}{E}\cos^2\alpha_1 \tag{2.40}$$

Perpendicular electric field After getting the motion of an ion in a parallel electric field, we also want to look at the motion of an ion in perpendicular potential gradients. Therefore, we choose a potential over the length of L along the z axis. The particle again only possesses kinetic energy of qeV_0. The potential along the original flight path is V_0 and it is linear in both directions along the electric field vector. Thus, we get the radial deflection force:

$$qeE = m\ddot{r}. \tag{2.41}$$

By simple integration with the starting parameters $r, z = 0$ we obtain

$$r = \frac{qeE}{2m}t^2. \tag{2.42}$$

By replacing t with $t = x/v_0$, where $v_0 = \sqrt{2qeV_0/m}$ is the initial axial velocity we obtain

$$r = \frac{E}{4V_0}z^2, \quad r' = \frac{E}{2V_0}z, \tag{2.43}$$

and therefore at the end of the potential at $r = L$

$$r_1 = \frac{E}{4V_0}L^2, \quad r_1' = \frac{E}{2V_0}L. \tag{2.44}$$

For small deflection angles α we can now replace the tangent with the angle and get the deflection angle with

$$\alpha = \frac{EL}{2V_0}. \tag{2.45}$$

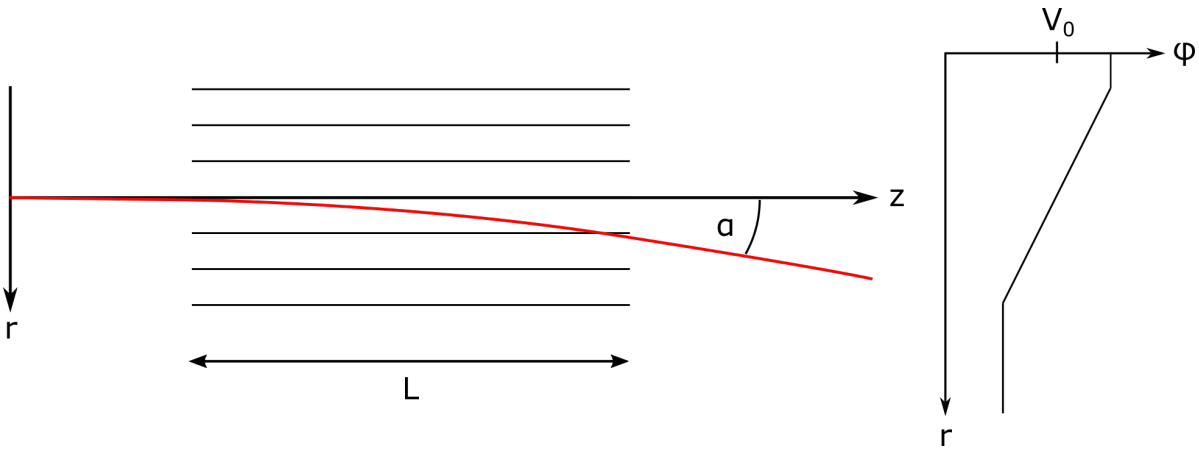

Figure 2.3: Trajectory (red) of a charged particle in a perpendicular electric field. The thin black lines indicate equipotential lines. Below, the potential along the r axis is shown. Adapted from [34].

Here we see that the flight path of a charged particle can be steered by suitable electric fields. However, this effect causes an energy dispersion, since α depends on the particle energy $E_{\text{ion}} = qeV_0$. This is not of concern for particles of different charge states accelerated by the same voltage. Even though they differ in kinetic energy, the differences drops out due to a stronger deflection force which also scales with qe, as seen above.

2.2.2 Electrostatic systems

The above described behaviour of charged particles in a potential landscape is already sufficient to describe all ion optical elements used in this work and also many more commonly used in different experiments.

A perpendicular electric field can simply be generated by a parallel plate capacitor along the beam. By combining two capacitors, one rotated by 90° with respect to the other one, one can steer the propagation direction in the whole plane.

On the other side, an electrostatic bender can be used to redirect the beam around corners, and also has a focusing effect on the beam [37]. In the following, a particular important component will be described: the einzel lens.

Einzel lens

One implementation to focus an ion beam is a so called einzel lens. It consists of three cylindrical electrodes along the beam axis, one inner and two outer ones. These outer ones are set to the same voltage. Typically, they are set to ground. The inner one is then set to either a negative or positive voltage.

Depending on the charge of the beam, these correspond to the two possible operation modes of the einzel lens: deccel-accel or accel-deccel. This refers to the ion velocity either being first accelerated and then decelerated by the voltage of the inner electrode or vice versa. In both cases, the velocity after the lens equals the velocity before the lens. In

the accel-deccel mode, the outer electrodes act as focusing lenses on the beam, while the inner electrode acts as a de-focusing element. In the deccel-accel mode, the roles are switched, and the inner electrode has the focusing effect. In the end, both modes achieve a focusing on the beam. However, the deccel-accel mode has a higher refractive power, due to the slower moving ions in the focusing element [32].

2.2.3 Deceleration in electrodynamic fields

Next to all electrostatic elements inside, the beamline is also equipped with one electrodynamic system. This is used to decelerate and bunch the ions. For this, a potential with a linearly increasing part is used. The potential along the flight axis z is given by an average potential ϕ_{avg} and the difference ϕ_{diff} between the upper potential and the lower potential.

$$\phi(t,z) = \Theta(t_s - t) \begin{cases} \phi_{\text{avg}} - \frac{\phi_{\text{diff}}}{2} & z < z_0. \\ \phi_{\text{avg}} + \phi_{\text{diff}} \left(\frac{z-z_0}{d_z} - \frac{1}{2} \right) & z_0 < z < z_0 + d_z. \\ \phi_{\text{avg}} + \frac{\phi_{\text{diff}}}{2} & z > z_0 + d_z. \end{cases} \tag{2.46}$$

Here, Θ is the Heaviside step function, depending on the time t and the switching time t_s, z_0 is the start of the linear increase and d_z is its length. The potential can be seen in the middle of fig. 2.6. The switching time is an experimentally chosen moment, when the whole potential is set to zero. The ions will lose the potential part of their energy and will be left with a lower kinetic energy. So if the switching time is set in such a way that the ions are located on the linear increasing part of the potential, the ions lose energy according to

$$E_{\text{loss}}(z) = qe \left(\phi_{\text{avg}} + \phi_{\text{diff}} \left(\frac{z - z_0}{d_z} - \frac{1}{2} \right) \right). \tag{2.47}$$

Thus, the ion cloud still has an energy spread leading to a distribution along the flight axis. Therefore, the loss of energy also depends on the energy of the individual ions. The position is given by $z(t) = v_{\text{ion}} t$ with the ion velocity from eq. (2.12). Considering that the energy spread to arise from the thermal distribution with $\Delta E = E_T$ like we did in section 2.1.4, we can calculate the spread in z to be

$$z(t_s) = v_{\text{ion}} t_s = \sqrt{\frac{2E_{\text{ion}}}{m}} t_s \quad \text{with} \quad \Delta z(t_s) = \sqrt{\frac{2}{mE_{\text{ion}}}} t_s \cdot E_T. \tag{2.48}$$

This leads to an energy loss according to

$$\Delta E_{\text{loss}}(z) = \frac{qe\phi_{\text{diff}}}{d_z} \cdot \Delta z(t_s). \tag{2.49}$$

Thus, we see that faster ions will climb higher up the potential and lose more energy than slower ions, who will lose less energy. Therefore, the energy distribution will become narrower.

2.3 The ideal Paul trap

Through the potentials inside the beamline described above, HCIs are transferred to the central piece of the experiment: a linear Paul trap. As mentioned in section 2.1, we still need a way of storing charged particles in accordance to Earnshaw's theorem. Therefore, the Paul trap makes use of a dynamic quadrupole potential switched with a radio frequency, hence why it is sometimes also called a quadrupole trap or radio frequency trap. In the following, the fundamentals of the Paul trap will be explained based on the description [9, 38]. The basis of the Paul trap is a quadrupole electric field. In a linear Paul trap, this is produced by four hyperbolically shaped electrodes. The general quadrupole potential has the form

$$\Phi_{\mathrm{QP}}(x, y, z) = \Phi_0(ax^2 + by^2 + cz^2). \tag{2.50}$$

The parameters a, b and c are constrained by the Laplace equation $\Delta\Phi = 0$, which yields $a + b + c = 0$. In a linear Paul trap, the quadrupole field is only two-dimensional, without any contributions along the z axis. Therefore, we have $z = 0$ and $a = -b$ and can simplify eq. (2.50) to

$$\Phi_{\mathrm{QP}}(x, y, z) = \Phi_0 \frac{x^2 - y^2}{r_0^2}, \tag{2.51}$$

with the spacing r_0 between the electrodes and the centre of the trap.

This potential forms a saddle-like structure, shown in fig. 2.5, and, in static form, is not yet usable to trap ions. In x direction, the ion encounters a potential barrier and consequently a force preventing it from escaping in this direction. In y direction, on the other hand, the potential drops, resulting in a force that drives the ions away from the trap centre. To achieve a confinement in both directions, the potential of the electrodes has to switch sign, leading to the same effects mentioned above, only in the other spatial direction. To achieve this inside a Paul trap, the quadrupole field will oscillate between these two configurations with the frequency Ω. Therefore, Φ_0 is made time dependent with an amplitude V_0 resulting in

$$\Phi_0(t) = V_0 \cos \Omega t. \tag{2.52}$$

For a correct frequency Ω, mostly in the radio frequency region, hence the name, a stable and closed trajectory of a charged particle inside the potential can be achieved. In this case, the ion will no longer experience the static quadrupole field, but a time averaged pseudo potential well. This leaves the z direction as the only direction with no trapping potential. Through additional electrodes inside the trap or along the hyperbolic electrodes, a static electric potential can be applied along the z axis, shown in fig. 2.4.

$$\Phi_z = \frac{\kappa U_z}{z_0^2} \left(z^2 - \frac{x^2}{2} - \frac{y^2}{2} \right). \tag{2.53}$$

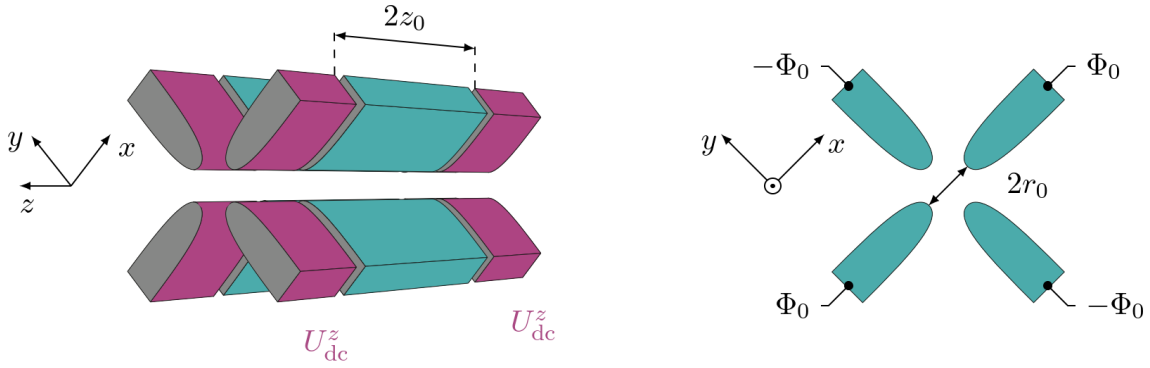

Figure 2.4: Geometry of a linear Paul trap with approximately hyperbolic trap electrodes. All electrodes are supplied with the quadrupole potential, while the segmentation allows a additional electrostatic potential supplied to the outer electrode (magenta), for axial confinement inside the central electrodes(cyan). Taken from[39].

This potential Φ_z depends on the voltage applied at these so-called DC electrodes, a geometrical factor $\kappa < 1$ and their distance to the trap centre z_0 Now, we can present the total potential in the trap centre, given by

$$\Phi(x,y,z,t) = V_0 \cos\Omega t \frac{x^2-y^2}{r_0^2} + \frac{\kappa U_z}{z_0^2}\left(z^2 - \frac{x^2}{2} - \frac{y^2}{2}\right). \tag{2.54}$$

From Newtonian mechanics and Maxwell's equations we know that a potential $\phi(t)$ exerts the force $\vec{F}$ onto a particle with mass m, changing its trajectory $\vec{r}$. Note that in the following Q denotes the charge state including the elementary charge with $Q = qe$, to distinguish it better from other parameters. This leads us to

$$\vec{F} = m\vec{a} \Rightarrow \ddot{\vec{r}} = \frac{\vec{F}}{m} = -\frac{Q}{m}\nabla\Phi(t). \tag{2.55}$$

From eq. (2.55), we can derive the equation of motion in x, y and z from the potential.

$$\begin{aligned}
\ddot{x} &= -\frac{2Q}{m}\left(\frac{V_0\cos\Omega t}{r_0^2} - \frac{\kappa U_z}{2z_0^2}\right)x, \\
\ddot{y} &= -\frac{2Q}{m}\left(-\frac{V_0\cos\Omega t}{r_0^2} - \frac{\kappa U_z}{2z_0^2}\right)y, \\
\ddot{z} &= -\frac{2Q}{m}\frac{\kappa U_z}{2z_0^2}z.
\end{aligned} \tag{2.56}$$

By defining the dimensionless parameters a and q

$$a_{x,y} = \frac{4Q}{m\Omega^2}\left(-\frac{\kappa U_z}{z_0^2}\right), \qquad a_z = \frac{8Q\kappa U_z}{m\Omega^2 z_0^2}, \tag{2.57}$$

$$q_{x,y} = \mp\frac{4QV}{mr_0^2\Omega^2}, \qquad q_z = 0. \tag{2.58}$$

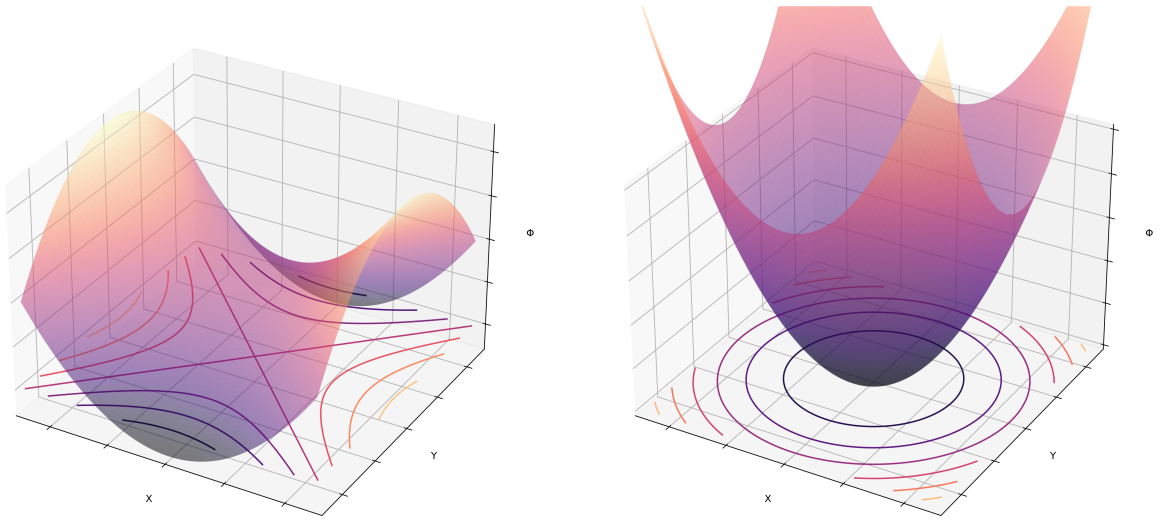

(a) (b)

Figure 2.5: **(a)** static quadrupole potential, resulting in a confinement in y direction. **(b)** pseudo potential of a Paul trap resulting from the time averaging of an oscillating quadrupole field.

we can simplify the equations of motion to:

$$\ddot{u} + \frac{\Omega^2}{4}(a_u - 2q_u \cos \Omega t)u = 0, \quad \text{with } u = x, y, z. \tag{2.59}$$

This is a so-called Mathieu equation. These offer two types of solution for the Paul trap: unstable solutions, where the trajectory grows exponentially, and stable solutions with closed trajectories. Most Paul traps are operated on a parameter region of a_u and q_u where the following is valid :

$$|a_u| \ll q_u \ll 1 \quad \text{for } u = x, y, z \tag{2.60}$$

This so-called adiabatic approximation features a small parameter subset for the stable solutions of Equation (2.59). Therefore, we can write down the approximate solution to the Mathieu equation:

$$u(t) = u_1 \cos \Omega_u t \left(1 + \frac{q_u}{2} \cos \Omega t\right). \tag{2.61}$$

Here Ω_u with its amplitude u_1 is the so-called secular frequency given by

$$\Omega_u \approx \frac{\Omega}{2}\sqrt{a_u + \frac{q_u^2}{2}}. \tag{2.62}$$

This solution allows a long storage of ions inside the trap centre. In a real trap, the storage time has restrictions due to real world effects like non-perfect vacuum or external heating of the ions. This can lead to a loss of the ion.

2.4 Laser cooling

To reduce the ion motion and gain longer storage times inside the Paul trap, a cooling method is needed to reduce the ions' energy. A suitable method is the direct laser cooling of an ion. To cool an atomic or ionic system via laser cooling, a specific level structure of the system is needed, which may not be present for every ion or atom. Therefore, also a second method, which does not rely on the ions' ability to be laser cooled, is discussed. The so-called sympathetic cooling, solves this problem by trapping an ion together with another -coolable- species, exchanging heat via Coulomb interaction. The description follows [40].

2.4.1 Doppler cooling

Doppler cooling is the most widely used laser cooling method to reduce the motion of trapped ions. The cooling process makes use of the momentum transfer caused by absorption and emission of photons. Not all ions are capable of being Doppler cooled. In order to be suitable, the atomic level structure needs to possess a transition that fulfils three criteria. Firstly, the transition needs to be fast decaying. Hence, most used transitions are dipole-allowed transitions. Secondly, the transition needs to be closed, meaning the excited state can only decay into one ground state, which can be exited again and not into a third state, which would leave the ion insensitive to the laser. The last criterium is that the transition has to be accessible by lasers. Thus, only transitions in or close to the optical regime can be used, excluding man transition e.g. in the x-ray regime.

If a photon with the right wavelength λ hits the ion, it can be absorbed, leading to excitation. Therefore, the ion gains the momentum of the absorbed photon p_γ given by

$$p_\gamma = \hbar k \quad \text{with} \quad k = \frac{2\pi}{\lambda}. \tag{2.63}$$

Because of the short lifetime of the excited state, the ion will quickly decay into its ground state, emitting a photon of the same wavelength resulting in a loss of the previously gained momentum. However, these two processes differ in one crucial detail. While the emission of the photon is isotropic, the absorption only transfers momentum along the propagation direction of the laser beam. If the deployed laser is now slightly detuned to a longer wavelength, the Doppler effect will make the ions more likely to absorb photons from the laser, if they move towards the laser. Hence, the velocity component in laser propagation direction is reduced, effectively slowing the ion down. If the laser beam is now aligned in such a way that it overlaps with all motional modes of the trapped ion in a Paul trap, all these modes are cooled. However, a Doppler cooled ion can only reach a certain limited temperature. Due to the constant scattering of light, the ion experiences momentum kicks of $\hbar k$. The minimum temperature that can be reached is called the Doppler limit. For Be^+ ions, this is $T_D = 302\,\mu K$ [39].

2.4.2 Sympathetic cooling

Nearly all HCIs, including, Ar^{14+} lack a suitable transition for Doppler cooling. Therefore, a second method is used to cool thermal energy of the HCIs. The so-called sympathetic cooling uses a second ion species, which will be co trapped with the HCI, to cool it. The simultaneously trapped ion needs to be laser-coolable. Through the Coulomb interaction between the two trapped ions, kinetic energy is transferred in between. One should note that the principle of sympathetic cooling is not limited to a laser-coolable ion, but can be extended to other cooling processes, due to its usage of a simple interaction between ions [41, 42].

2.5 Retrapping concept

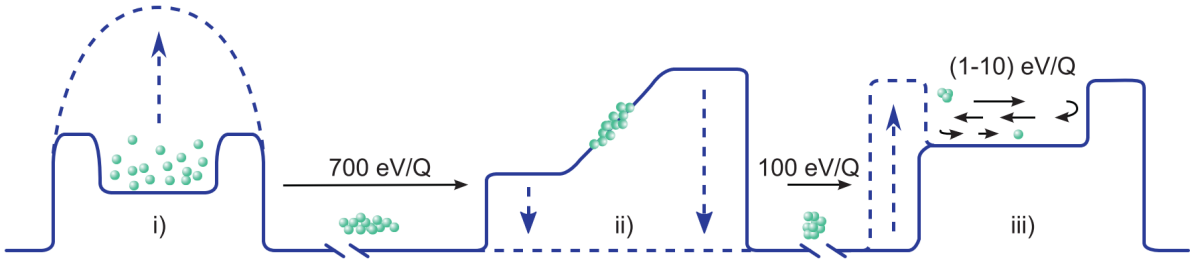

Figure 2.6: Schematic depiction of the potential landscape of the experiment, including the time varying potentials (dashed) along the flight path (black) of the ions (cyan). Taken from [15].

All physical principles mentioned above will be combined in the retrapping scheme used for this work [15]. First, HCIs are produced in an EBIT, guide them through a beamline and trap them inside a Paul trap. This process is depicted in fig. 2.6 as a scheme of the potential landscape. First, they are produced in an EBIT reaching high charge states by EII and evolving according to eq. (2.9). Being kicked out of the EBIT via a kick potential, the ions move along the beamline, experiencing refocusing and steering. Through precise timing inside the PDTs the ions lose most of their kinetic energy. In a second step, the kinetic energy is reduced further, by biasing the whole Paul trap to a higher potential. The last step to stop HCIs inside the Paul trap is to sympathetic cool them via Be^+ ions inside the trap. This is done by a so-called Coulomb crystal of Be^+ ions inside the trap.

These are spatially ordered structures of trapped ions that form if these ions are cooled to a sufficiently low temperature [43]. In this case, the ions form structures based on their repulsion and the surrounding potential. The temperature limit T_{CC} for crystallization depends essentially on the kinetic energy and the inter-particle Coulomb energy. For singly charged ions trapped inside a Paul trap, this leads to the required temperature T of $T \leq T_{CC} \approx 10\,\mu K$ [43].

With such a crystal present in the trap, the HCIs are injected into the trap. To achieve sufficient interaction time between the HCIs and the crystal, a multipass concept with reflections at the end of the trap axis is employed. Using electrodes with higher potential, the HCIs fly along the trap axis until the Be^+ crystal, effectively acting like a source of friction, stops the HCIs. To reach a significant amount of stable reflections without the loss of the HCIs, their residual kinetic inside the Paul trap needs to be around $1 \times q$ eV, as shown by simulations in [44]. For this kinetic energy, an interaction length around 220 mm is needed. With an average ion crystal size around 0.5 mm for large crystals, this leads to the requirement of more than 500 reflections inside the trap. After sufficient sympathetic cooling, HCIs get stuck inside the Be^+ crystal and co-crystallice inside the Paul trap.

3 Experimental setup

The experiments carried out for this work take place at the cryogenic Paul trap experiment CryPTEx-II. It is the successor to CryPTEx and therefore shares its conceptual basis of producing HCIs inside an EBIT, transporting them through a beamline and trapping them inside a cryogenic Paul trap [23]. Additionally, it features improvements like the room temperature compact EBIT or the superconducting radio frequency (RF) cavity [21, 18]. The setup of the complete experiment can be found in [39].

In the following chapter, components necessary to trap HCIs inside the Paul trap are explained, section 3.1 introduces the beamline its electrodes and section 3.2 describes the cryogenic Paul trap and its surroundings. While the whole experiment consists of three sections, the EBIT, the Beamline and the Paul trap itself, only the latter two were investigated and altered in the work of this thesis. The EBIT was already steadily producing HCIs and was fully operational. For a closer look at the EBIT, see [30].

3.1 Beamline

Connecting the EBIT and the Paul trap, the beamline is the central experimental part for transporting and precooling the HCIs. The beamline used in this work was built by M.K. Rosner [30], based on the original beamline used in CryPTEx by L. Schmöger [32] which was developed further by P. Micke [45]. It consists of five Sikler lenses (SL), an electrostatic bender and a pulsed drift tube. These components are all located inside a vacuum system pumped by turbo molecular pumps. The beamline already features micro-channel plates for beam diagnostics, which will be explained later on. The description given here follows [30].

3.1.1 Sikler lens

A Sikler lens is a specially designed einzel lens, built to gain more control over the ion beam than with a simple einzel lens [46]. Hence, it is build from three electrodes, with the outer electrodes grounded, and the inner electrode set to a certain voltage to achieve the focusing effect of an einzel lens. This inner electrode is split into four parts by two orthogonal cuts, 45° askew from the symmetry axis. Therefore, we end up with four electrodes, which are referred to by their position seen from the incoming beam: LO(engl.: left up), RO(engl.: right up), LU(engl.: left down), RU(engl.: right down). These extra electrodes can be used to affect the beam in different ways rather than just to focus it. Therefore, we end up with four degrees of freedom.

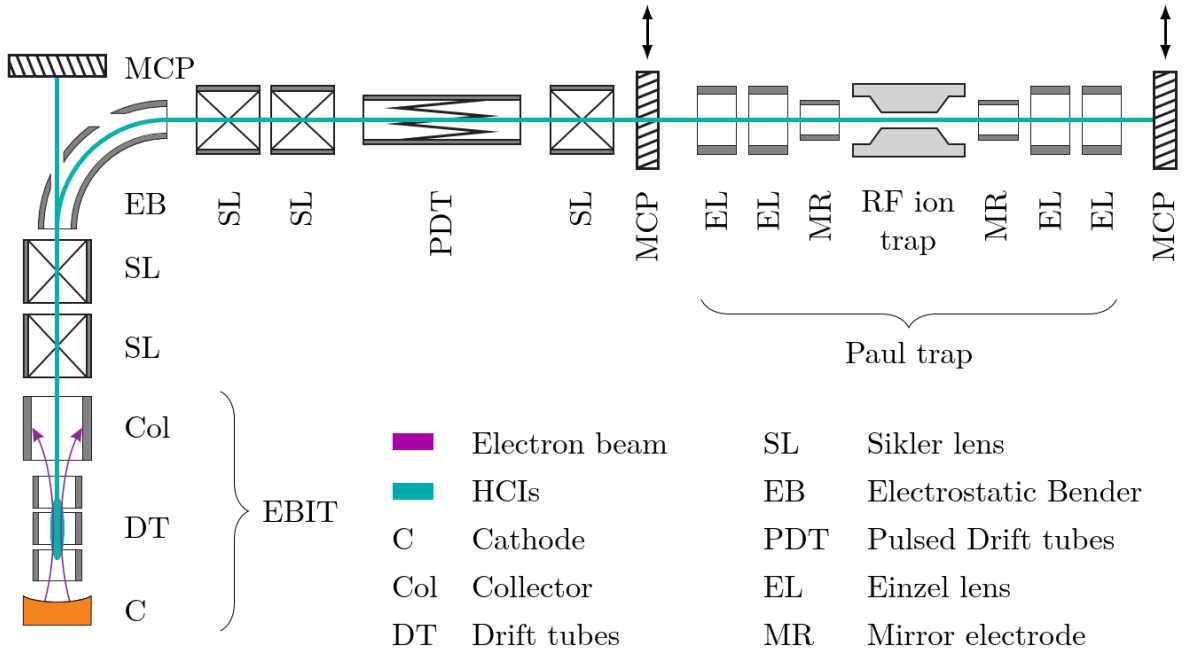

Figure 3.1: Schematic overview of the used setup, including all major electrodes used in this thesis. Taken from [39].

- **Focus:** By setting all four electrodes to a certain voltage, one can use a Sikler lens as a classical einzel lens, which will simply focus the beam.

- **Steering:** By grouping two neighbouring electrodes, a Sikler lens can be used to steer the beam. The effect depends on the charge of the electrodes. E.g., biasing LO and RO to a higher voltage, the beam will be steered downwards, so along the normal vector of the resulting separation plane. BY grouping LO+RO and LU+RU, one can steer in the vertical direction, and by grouping LO+LU and RO+RU, in the horizontal direction. Therefore, we have full control over the propagation direction of the beam.

- **Astigmatism:** By grouping opposite electrodes, one can control the astigmatism of the beam. Therefore, astigmatisms of the beam can be compensated by the Sikler lenses. In the orientation described above, only the astigmatism turned 45° to the horizontal plane can be corrected. Therefore, SL3 is turned 45° to also address the left astigmatism axis.

The different Sikler lenses are operated in the deccel-accel mode described in section 2.2.2. One should note that all these operations can be imposed over each other.

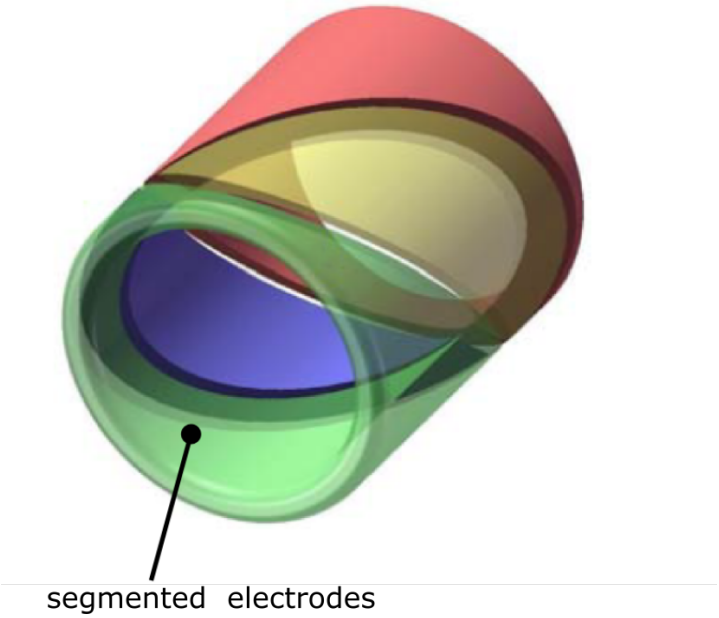

Figure 3.2: Schematic representation of the segmented inner electrode of a Sikler lens. Taken from [30].

3.1.2 Bender

After the first two Sikler lenses, the ions have to be deflected in an 90° angle. Therefore, an electrostatic bender is employed [37]. This bender is made of two hollow cylinders of different radius and different height. The bender also has a focusing effect on the ion beam. For diagnostic purposes, the bender has an opening aligned with the EBIT, allowing the detection of ions on the first MCP.

3.1.3 Pulsed drift tubes

The electrodynamic potential presented in section 2.2.3 is supplied by the pulsed drift tubes (PDT). It consists of two cylindrical tubes with a serration in between. By applying different voltages to the tubes, one can achieve the linear increasing electrical potential described in Section 2.2.3, because their share in circumference linearly changes along the beam direction. Both electrodes PDT electrodes are switched to ground by a high voltage switch while the ions fly through the PDTs [32].

3.1.4 Micro-channel plate

In addition to the mentioned manipulation methods and control mechanism, one needs a method to evaluate and characterize the ion beam. Micro channel detectors are employed at different positions along the beamline. MCP detectors consist of a metallic plate with small perforations which are tilted in respect to the surface. While the bulk material has

a high resistance, the front and the back of the MCP are made of conductive material to form two electrodes. In this experiment, these holes have a diameter of around 50 µm and an inclination of around 8°. These channels act as electron multipliers. An incoming particle hits the inside of the channels, releasing electrons from the detector. These get then accelerated inside the channel by a high voltage applied between the front and the back of the MCP and hit the inner wall again, starting a cascade of secondary electrons. The MCP used in this experiment consists of two plates stacked upon each other. The inclination of the channels are mirrored in comparison to each other, resulting in a chevron configuration. This allows for a higher amplification of the incoming signal [47] After the two micro-channel plates, an anode is connected via a fast pre-amplifier (Model: ORTEC VT120) to an oscilloscope (Model: Tektronix TDS2024C), which is used to read out the signal in the form of a voltage peak. This setup allows no spatial resolution of the ion beam. However, it offers a temporal resolution up to a ns scale, needed to resolve the temporal differences between different charge states.

Three MCPs exist inside the experiment. MCP1 located behind the bender in direct line to the EBIT, for first detection of the extracted ions. MCP2 in front of the Paul trap, after the PDTs and MCP3 behind the Paul trap to detect if the beam is correctly aligned with the trap.

Additionally, MCP2 has a retarding field analyser installed in front of it. This analytic tool is used to measure the energy and the energy spread of the ions. It consists of two meshes directly in front of the MCP. While the first mesh is grounded, the second one can be set to an arbitrary voltage, so only ions with a kinetic energy high enough can pass the potential of this mesh.

3.2 Paul trap environment

The cryogenic Paul trap used in CryPTEx-II is a linear Paul trap, based on [44] but developed further by J. Stark [39], by combining it with a super conducting radio frequency cavity. The individual parts are explained following [18].

3.2.1 Radio frequency cavity

The heart of the whole experiment is the cryogenic Paul trap, which combines a linear Paul trap with a superconducting resonator cavity to produce extremely stable RF potentials at a resonance frequency of around 35 MHz. This enables the trapping of ions in a very stable environment with very little noise on the ion motion.

Cryogenic setup

The whole cavity needs to be in a cryogenic environment, consisting of an outer stage cooled to 40 K and an inner stage cooled to 4 K. These stages form two heat shields around the trap, suppressing heating by black body radiation. Inside the 4 K stage, the niobium resonator is located, cooling it below niobiums critical temperature of 9.25 K.

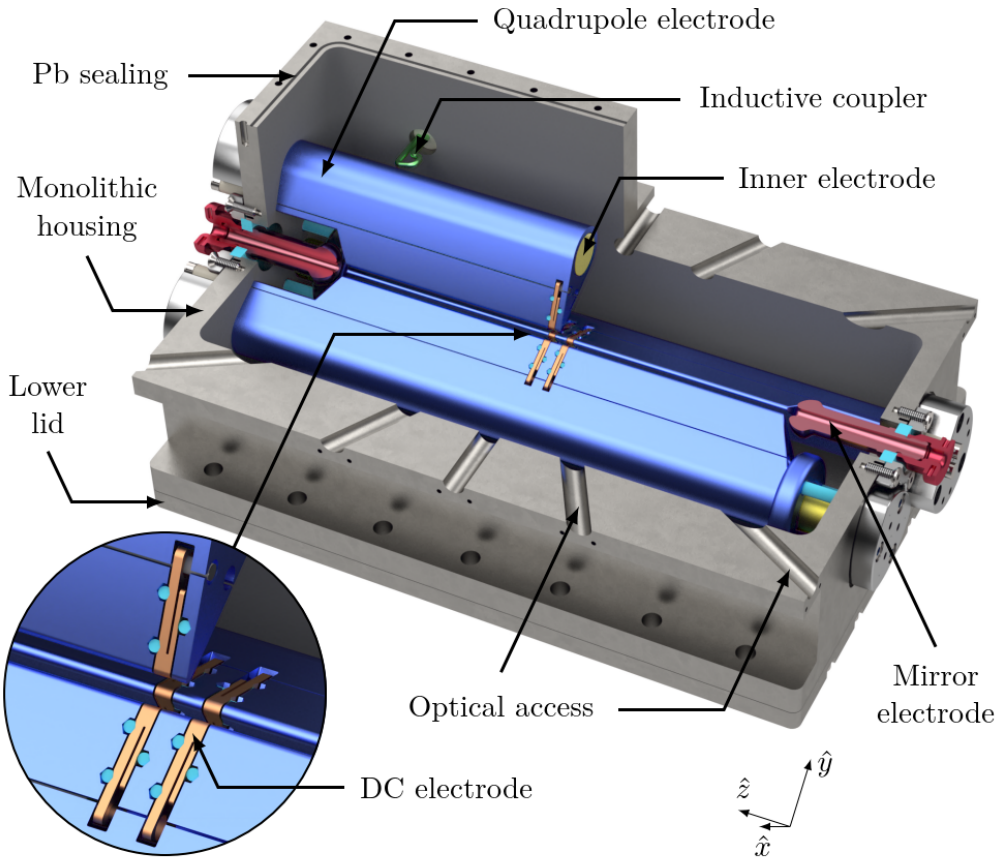

Figure 3.3: Cross-section of the Paul trap with its electrodes inside the superconducting cavity. Taken from [39]

Low temperature also benefits the vacuum inside the trap by freezing out residual gas on the walls [48].

The heat shields feature ports needed to provide access to the trapped ions. The ports along the trap axis feature additional einzel lenses to focus the incoming HCI beam.

RF electrodes

The quadrupole potential is supplied by four electrodes with a cone like cross-sections. They consist of an outer and an inner part fixed to the cavity wall and opposite charge to cause a large capacity. This is needed to ensure the right trap parameters while keeping the needed RF frequency low.

DC electrodes

Axial confinement of the trap is provided by eight DC electrodes embedded into the quadrupole electrodes. In addition to supplying the axial confinement, each of the

electrodes can be biased independently to correct the potential of the trap for inhomogeneities.

3.2.2 Mirror electrodes

Two electrodes are placed along the flight path of the HCIs, in front of the Paul trap electrodes and behind the Paul trap. These are the so-called mirror electrodes, which are used to reflect the HCI bunch back and forth along the trap axis, hence the name mirror electrodes. The electrodes are placed 155 mm apart and are essential for the re trapping concept used in this work. For this, the mirror electrodes need a precise timing to allow the ion bunch to enter the trap, while also raising their potential quick enough to enclose the ions inside the RF field. However, here we face a conflict concerning the mirror electrodes. These electrodes, which can be simplified as an RC circuit, are charged from ground to U_s up according to,

$$U_c = U_\mathrm{s}(1 - \exp\left(\frac{1}{\tau}\right)). \tag{3.1}$$

Therefore, a small time constant τ is desired. This time constant τ is given by $\tau = RC$, with the capacity C and the resistance R [49]. However, to ensure that the mirror electrodes don't couple out a significant amount of RF Power, due to their proximity to the RF electrodes, they are connected to their voltage supplies via a large resistance. This forms an RC-circuit with the capacity between the mirror electrodes and the trap, leading to a low pass filter, blocking the RF. A prior conducted thesis determined the time constant τ to be at $\tau_1 = 114\,\mu\mathrm{s}$ for the first mirror electrode and $\tau_2 = 152\,\mu\mathrm{s}$ [50]. This leads to a cut-off frequency of the low-pass filter of $f_c = \frac{1}{2\pi\tau} = 1.4\,\mathrm{kHz}$, guaranteeing a sufficient RF blocking. However, an expected time of flight of an ion inside the Paul trap is around $40\,\mu\mathrm{s}$ [44]. Therefore, a precise timing will be needed to confine the HCIs inside the Paul trap.

3.2.3 Beryllium setup

To employ laser cooling like described in section 2.4 and subsequently sympathetic cooling HCIs, a source of Be^+ ions and a cooling system is needed.

Beryllium source

The CryPTEx-II experiment features a beryllium oven. Here, a small beryllium sample is surrounded by a tungsten wire. By heating the tungsten wire electrically, beryllium atoms sublimate into the vacuum. The thermal beam of Be atoms get collimated by several apertures and directed into the trap centre.

Laser setup

Here, the beryllium beam gets superimposed with a photo-ionization laser. As the name implies, this laser is used to ionize the beryllium, so it can be trapped inside the Paul

trap. However, the ionization energy of beryllium is 9.32 eV, which corresponds to a laser wavelength of 133 nm. A laser with such a short wavelength is difficult to operate. Therefore, the atoms get ionized via an intermediate excited dipole allowed state, which can be addressed by a 235 nm laser. An absorption of a second photon of this ionization laser will lead to ionization of the electron in the excited state, leaving us with the wanted beryllium ion.

These produced ions still need to be laser-cooled. Thus, a laser with a wavelength of 313 nm is aimed at the trap centre. This laser can drive the $^2S_{1/2}$ to $^2P_{3/2}$ transition of the beryllium ion. This transition fulfils nearly the requirements for laser cooling by being a fast decaying transition. However, it is not a closed cycle, as the ground state has a hyperfine structure, splitting the ground levels by 1.25 GHz due to the nuclear spin into F=1 and F=2. Therefore, a part of the laser beam is separated, shifted by 1.25 GHz by using acustooptical modulators and superimposed with the main cooling beam again. This laser then depopulates the upper hyperfine state and ensures a closed laser cooling transition.

3.2.4 Imaging system

To generate images of the final Coulomb crystal inside the Paul trap, an imaging setup is installed at CryPTEx-II collecting the fluorescence light coming from the laser cooled beryllium. A stack of lenses is set up directly at the 4 K stage of the experiment, extracting light from the centre of the trap. It focuses the light onto a detection system above, consisting of a photomultiplier tube and an EMCCD (electron multiplying charge coupled device) camera. Only the latter one is used for the experiments carried out in this thesis. It can provide information about the position and configuration of the ion crystal inside the trap. For more information on the imaging system, see [51].

4 Beamline optimization

The experimental part of this work is grouped into two chapters, one concerning all processes happening inside the beamline to prepare an ion bunch of maximal intensity arriving at the trap, and one trapping the HCIs inside the Paul trap.

Optimization of the beamline was done in order of the elements of the beamline starting from the EBIT. The EBIT itself was already running steadily, because of optimizations by Alvaro Garmendia as a part of his bachelor thesis [50]. The main goal in the following section was to produce a bunched beam of highly charged argon ions of one charge state with a low enough kinetic energy for later retrapping in the Paul trap. Therefore, highly charged argon ions were bred inside the EBIT, extracted into the beamline, their charge state identified and selected and finally decelerated inside the pulsed drift tubes.

4.1 Sikler lens and Bender optimization

As mentioned above, the experiment started with a running EBIT. The drift tube voltages were already set, so a steady yield of ions was produced. To get the wanted argon ions, argon gas was injected via the injection system with a pressure of 1×10^{-7} mbar to ensure a sufficient ion amount. To extract the ions from the trap, the central drift tube was pulsed via a high voltage switch to a Voltage of around 695 V. This extraction was first done with a repetition rate of 3 Hz, thus defining the breeding time of the HCIs. These initial parameters were taken from previous work [50] and were later altered to optimize for the yield of the selected ions. The voltages used for the EBIT were:

Electrode	Cathode	Focus	Anode	Kick potential
Voltage	650 V	925 V	200 V	695 V

Table 4.1: Voltages settings applied to different electrodes of EBIT. They define the electron beam energy of the EBIT and the kinetic energy of the HCIs extracted from the trap.

Electrode	DT1	DT2	DT3	DT4	DT5	DT6
Voltage	200 V	540 V	570 V	539 V	570 V	0 V

Table 4.2: Voltages settings applied to the drift tube (DT) inside the EBIT trap centre, defining the axial tap depth. For further information, see [50].

These parameters ensure production of a large range of argon ions, with an electron beam energy of 1125 V. The beam is energetic enough to produce ions up to Ar^{16+}, with its ionization energy of 4123.665 57(4) eV being the first to exceed the beam energy [52].

In the following part, precise timing of electrodes synchronized to the extracted ions is needed. To achieve this, a global timestamp, denoted as t_0, is established by one function generator to trigger all other function generators. Thus, all following timestamps and measurements refer to t_0 as their zero point. The frequency of generating the t_0 signal therefore marks the extraction rate of the EBIT. The first relevant event is at $t_{\text{kick}} = 1350.2\,\mu\text{s}$, when the potential of the central drift tube of the EBIT gets raised to the kick potential ϕ_{kick}, leading to the axial extraction of the produced HCIs. The temporal gap had to be chosen this long due to the mirror electrodes and especially the first mirror electrode. Technical issue constrained the switching, hence the electrode was switch at t_0 and had to settle to the right voltage. Combined with the time constant mentioned in section 3.2.2, we used a longer waiting time to ensure that transient processes are no longer a concern.

After exiting the EBIT, the HCIs pass the first two Sikler lenses, fly towards the bender and can be detected at the first MCP sitting behind the hole in the bender, see section 3.1. To achieve a signal as good as possible, each of the four voltages (see section 3.1.1)of each Sikler lens of the setup needs to be optimized. Hence, an optimization algorithm for the Sikler lenses was implemented. With the help of this automation, every Sikler lens later on was optimized multiple times until the signal showed no significant improvement any more. Even though this routine is fairly straight forward, the gain through this procedure was immense, therefore it is shortly addressed here:

Initially, all Sikler lens electrodes after the Sikler lens desired to optimize and before the MCP used to read out the signal are set to $V_0 = 200V$. Thus, they already acted as an einzel lens on the beam, which was already enough to receive at least some signal. The algorithm used the four degrees of freedom described in section 3.1 by first optimizing the horizontal steering, then the vertical steering, then the focus setting and afterwards compensating the astigmatism. Thus, a parameter array was defined for each operation by a deviation in positive V_{max} and negative V_{min} "direction" from V_0 and a step size.

For optimization of the horizontal steering, the electrodes LO and LU were grouped together to form an effective left laying electrode and RO and RU to form a right electrode. The voltages of L were iterated from $V_{\text{inital}} = V_0 + V_{\text{min}}/2$ to $V_{\text{final}} = V_0 + V_{\text{max}}/2$ while the voltage of R was iterated from $V_{\text{inital}} = V_0 - V_{\text{min}}/2$ to $V_{\text{final}} = V_0 - V_{\text{max}}/2$ simultaneously. At every iteration step, the voltage signal from the MCP was recorded by an oscilloscope. The maximal voltage of the signal was used as a measure of the intensity of the ion bunch. To gain sufficient statistics, 30 extractions were recorded per iteration. After iterating through the whole parameter array, the best settings were chosen as the new V_0 of the electrodes. The vertical steering was optimized by the same routine, only the electrodes were grouped differently into an up electrode LO and RO, and a down electrode LU and RU. The optimization of the focus is simpler. Here, all electrodes are simply iterated from $V_{\text{inital}} = V_0 + V_{\text{min}}$ to $V_{\text{final}} = V_0 + V_{\text{max}}$. To compensate the astigmatism, the electrodes were grouped differently. Here, RO and LU, and RU and LO were altered simultaneously. Nevertheless, it follows the same principle as the steering optimization.

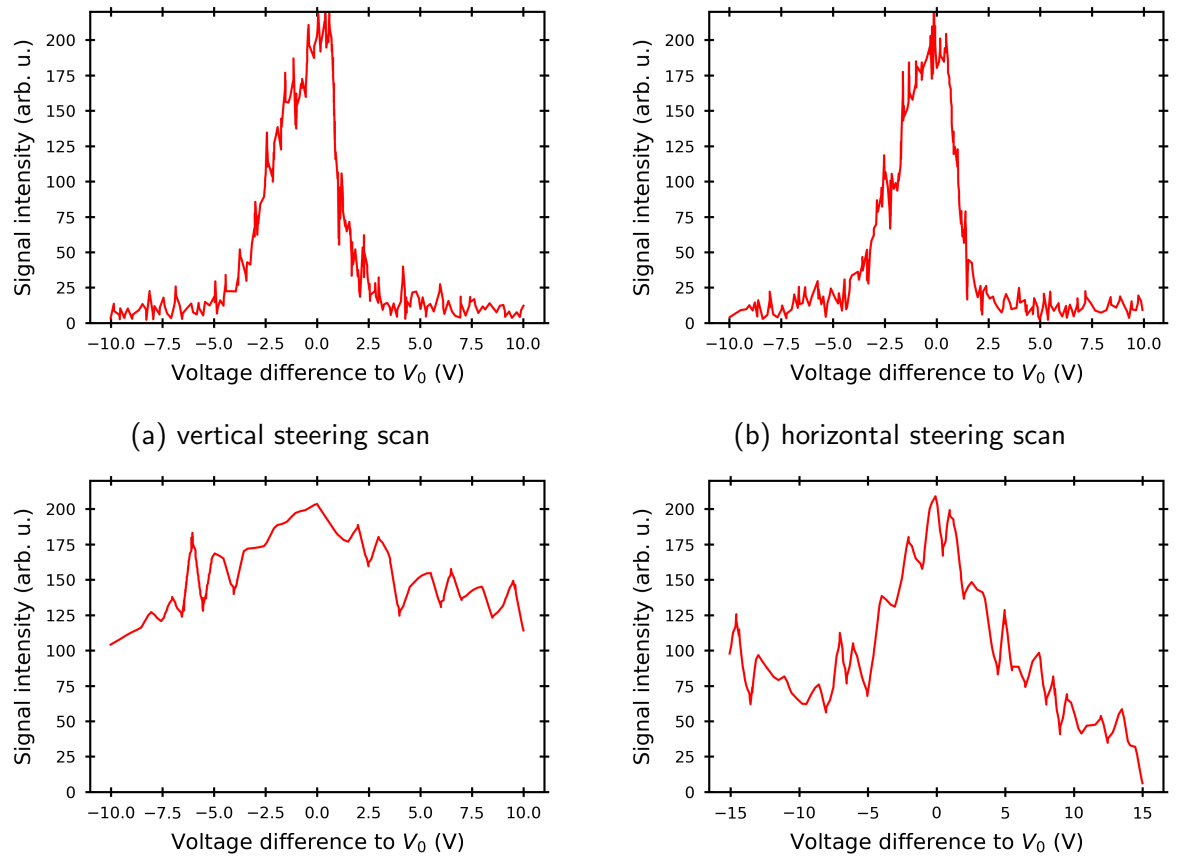

Figure 4.1: Dependency of the ion signal on different beam manipulations following the optimization algorithm performed on SL5. Note that V_0 for these scans was $V_0 = (83.85\,\mathrm{V}, 84.25\,\mathrm{V}, 92.25\,\mathrm{V}, 85.15\,\mathrm{V})$ for the electrodes LO, RO, LU, RU respectively. A clear maximum for each manipulation can be seen, also showing different levels of sensitivity for the individual optimization steps.

After a full run of the program, a new set of voltages for the electrodes was found. If the development of the signal indicated that the maximal intensity was not yet reached, the program could just be started again now optimizing around the new set of voltages. One should note that this algorithm may not find the global maximum of signal intensity in the whole parameter space of the beamline. Nevertheless, it offered a more systematical approach and a more reliable optimization; between bunch variations of signal strength and therefore ion yield made it nearly impossible or at least a guessing game to try to optimize the settings by hand. As an example of the dependency between the signal intensity and the optimization of the four degrees of freedom, fig. 4.1 shows the signal at MCP3 while optimizing SL5. The setting concerning both steering effects show significant and strong impact on the signal. The focus and astigmatism corrections showed less effect on the signal, but still contributed to a higher intensity.

With the procedure described above, SL1 and SL2 were now optimized to produce a good signal at MCP1. After optimizing each Sikler lens multiple times, the parameters displayed in table 4.3 were found. Following up SL1 and SL2, the bender was the next

Electrode	SL1LO	SL1RO	SL1LU	SL1RU	SL2LO	SL2RO	SL2LU	SL2RU
Voltage	154 V	119 V	151 V	176 V	220 V	180 V	220 V	180 V

Table 4.3: Voltages applied to Sikler lens 1 and 2. These values were found after multiple iterations of the above described algorithm.

component to be adjusted. Therefore, MCP2, directly in front of the Paul trap, was used as read out. The bender, in contrast to the Sikler lenses, was adjusted by hand. The voltage of the inner (BENDER-) and outer electrode (BENDER+) were tuned until a good signal was achieved at MCP2.

Electrode	Bender +	Bender -
Voltage	137V	-196V

Table 4.4: Voltages applied to the bender electrodes for optimal beam steering around the 90° corner.

4.2 Charge state selection

Until now, the ion bunch still contains all charge states produced inside the EBIT. These different charge states can also be seen on the MCP signal. An important parameter determining which charge states are produced in the EBIT is the breeding time (inverse of the extraction rate), which is easily adjusted. Therefore, we should be able to see different charge states by iterating over different extraction rates. As we have seen in section 2.2, the only difference for ions of different charge states in our electrostatic setup is the time of flight (TOF). The arrival of different charge states at different times can be seen at MCP1. In fig. 4.2 the extraction rate was varied to see exactly this phenomenon.

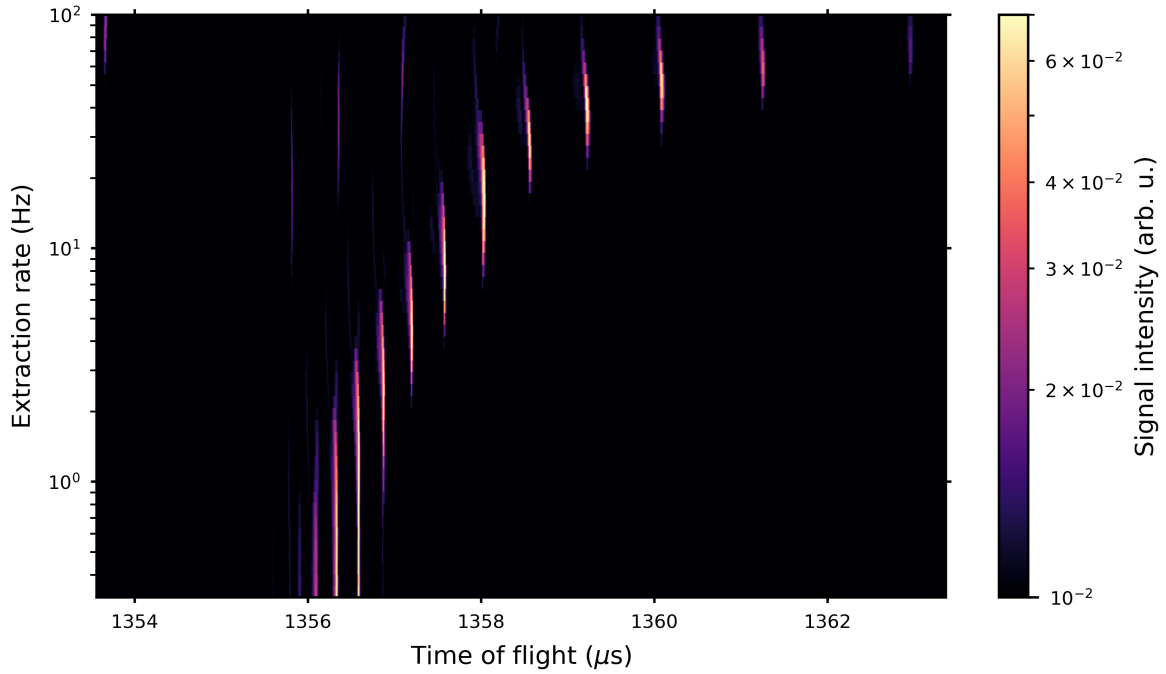

Figure 4.2: Time of flight spectrum for different extraction rates between 0.3 Hz and 100 Hz detected on the first MCP. All EBIT parameters were still unaltered from the parameters mentioned above. An array of strong signal are noticeable, corresponding to different charge states of argon ions. Also, above the supposed argon array, a fainter array of peaks is detectable. This could be ions produced from residual gas like oxygen or nitrogen left in the trap.

In this plot, different lines for different charge states can be seen. Also, some residual gas can be seen in the plot. A faint series of lines is visible at higher extraction rates than the intense argon lines. However, these signals, probably coming from residual gas inside the system, can easily be excluded with the correct combination of timing and extraction rate. fig. 4.2 shows that ions of different charge state can be distinguished by their time of flight. We utilize this time difference to select the desired charge state at SL3. First SL3 is tuned such that the signal is optimal at MCP2 in front of the trap.

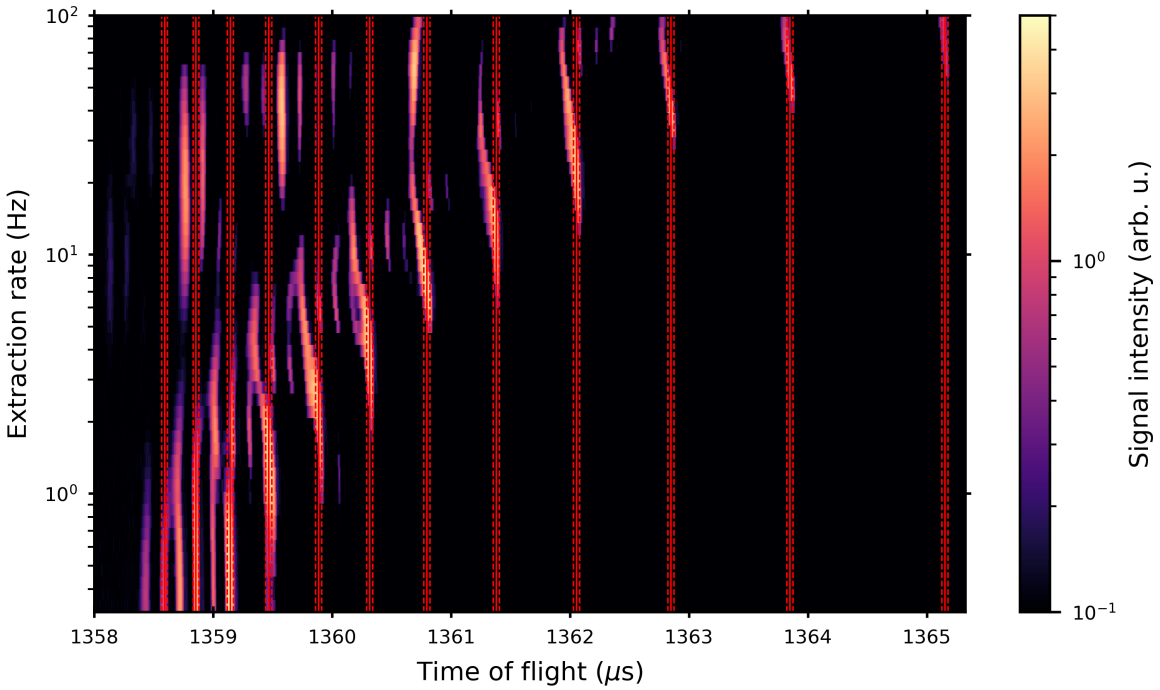

Figure 4.3: Time of flight spectrum for different extraction rates between 0.3 Hz and 100 Hz detected on the second MCP. The mean time (red, solid line) of flight of the prominent lines and their errors (red, dotted line) are shown. For these fits, see fig. 4.4. Here, the distinction between a line featured in the upper or lower array is more visible. However, this detector seems to feature spectra with more artefacts than fig. 4.2. Apparently, high signal intensities sometimes produced reverberations in the signal.

To exploit the different TOFs for each charge state, one SL3 electrode is connected to its voltage supply via a fast high voltage switch. We chose SL3R as the switching electrode. The switch is now triggered by a function generator in such a way that only while the wanted ion specimen is flying through the lens, it is set to the correct voltage. Any other time, one electrode is grounded, and therefore the beam is steered into the wall of the vacuum chamber. One should also notice that SL3 is tilted by 45° with respect to the remaining Sikler lenses. Hence, also the astigmatism of the beam in the remaining axis can be compensated. The optimal parameters of SL3 were found as listed in table 4.5

Electrode	SL3L	SL3O	SL3R	SL3U
Voltage	394 V	406 V	394 V	406 V

Table 4.5: Voltages applied to Sikler lens 3.

To identify the different charge states and the correct switching time, the same measurement as in fig. 4.2 is made, with the only difference that now we measure the

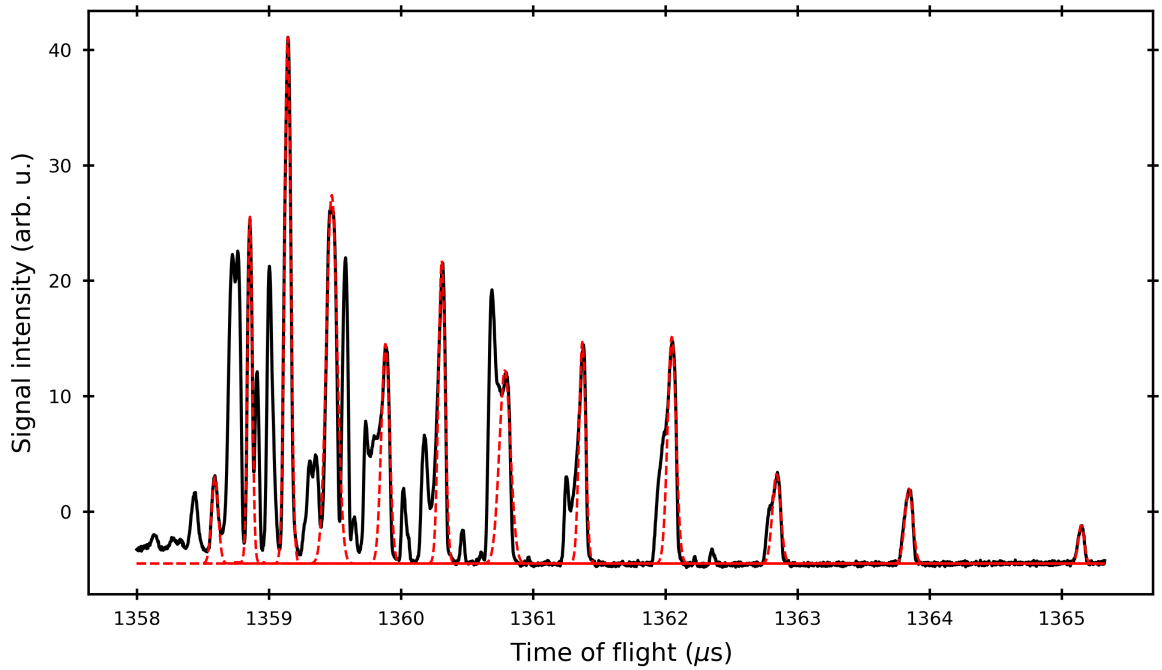

Figure 4.4: Time of flight spectrum detected on the second MCP. Signal(black) integrated over the extraction rate, ranging from 0.3 Hz to 100 Hz. Gaussian curves (red) fitted to the individual peaks of the signal, representing argon peaks.

TOF-spectrum with MCP2. In fig. 4.3 already the mean time of flight and its errors are shown, which originate from a Gaussian fit, see fig. 4.4.

By integrating the signal over all extraction rates, a plot with signal intensities over the time of flight is extracted. This signal shows many peaks, not all coming from Argon ions. Gaussian curves were fitted to the supposed argon signal to extract their TOF and the error as the standard deviation of the Gaussian. The individual selection if a signal is generated by argon ions, residual gas or detector artefacts is done comparing fig. 4.2 and fig. 4.3. Comparing between these two images, also a shift of the time of flight for higher extraction rates can be seen. This also leads to secondary peaks in the signal. To extract the individual charge states for the individual lines, we modify eq. (2.28) to read

$$t_a = t_0 - \frac{t_b}{\sqrt{q}} \tag{4.1}$$

to allow an offset t_0. Now we fit this function to our TOFs.

In fig. 4.5 we see that indeed we are able to produce all argon charge states between Ar^{5+} up to Ar^{16+}, as we already expected from the EBIT parameters in section 4.1.

Through the identification of the charge states, we can also take a look at the charge state distribution depicted in fig. 4.6. This helps to determine the most efficient extraction rate. However, this plot is the signal changing for different extraction rates along the mean time of flight. Therefore, this plot underestimates the signal of each charge state at higher extraction rates, due to the shifts of the time of flight recognizable in fig. 4.3.

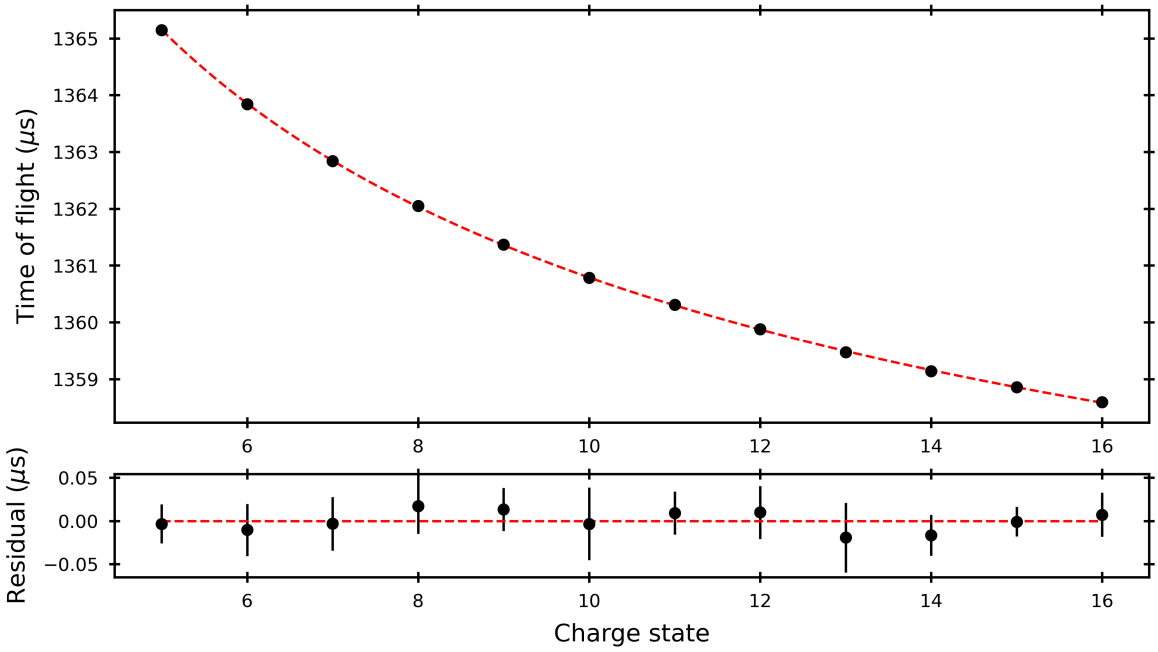

Figure 4.5: Time of flight (black) of argon ions as a function of the respective charge state, with the fit function following Equation (4.1). The residuals shown below indicate a good concordance between the found fit and the identified charge states.

Now we decided to select Ar^{14+}, trying to separate this charge state from other different charge states. We see a distribution expectable from section 2.1.3 and a maximal abundance of Ar^{14+} at 0.26 Hz. Nevertheless, we ultimately chose 0.7 Hz as the extraction rate for the system. The main reason for this was that a lower extraction rate would lead to a much longer evaluation time for the following measurements. With the optimization of the Sikler lenses already taking hours at 3 Hz, this would unnecessarily prolong the procedure. Moreover, other experiments pursuing the goal of HCI retrapping used similar frequency for retrapping attempts. Overall, this is limited with regard to higher frequencies by a minimal interaction time the HCIs later need inside the Paul trap to be cooled sympathetically [45]. Also, taking the still strong signal into account, 0.7 Hz seemed a quite reasonable choice. It should also be noted, that the optimal extraction is also influenced by other parameters of the EBIT. A higher pressure inside the EBIT can lower the optimal extraction time, due to the presence of more residual gas, leading to increased charge exchange. In our case the EBIT was only pumped for about a week without heating out residual water inside the vacuum chamber which lead to a higher than usual pressure in the trap. However, this will slowly sink over time, shifting the optimal extraction rate higher.

After the identification of Ar^{14+}, a signal generated was set up, so the above-mentioned switching mechanism only selected Ar^{14+}. Therefore, two timings (A, B) were selected. One for switching the SL3 electrode from ground to the right voltage setting, and a second one for switching the SL3 electrode back to ground. After these settings were

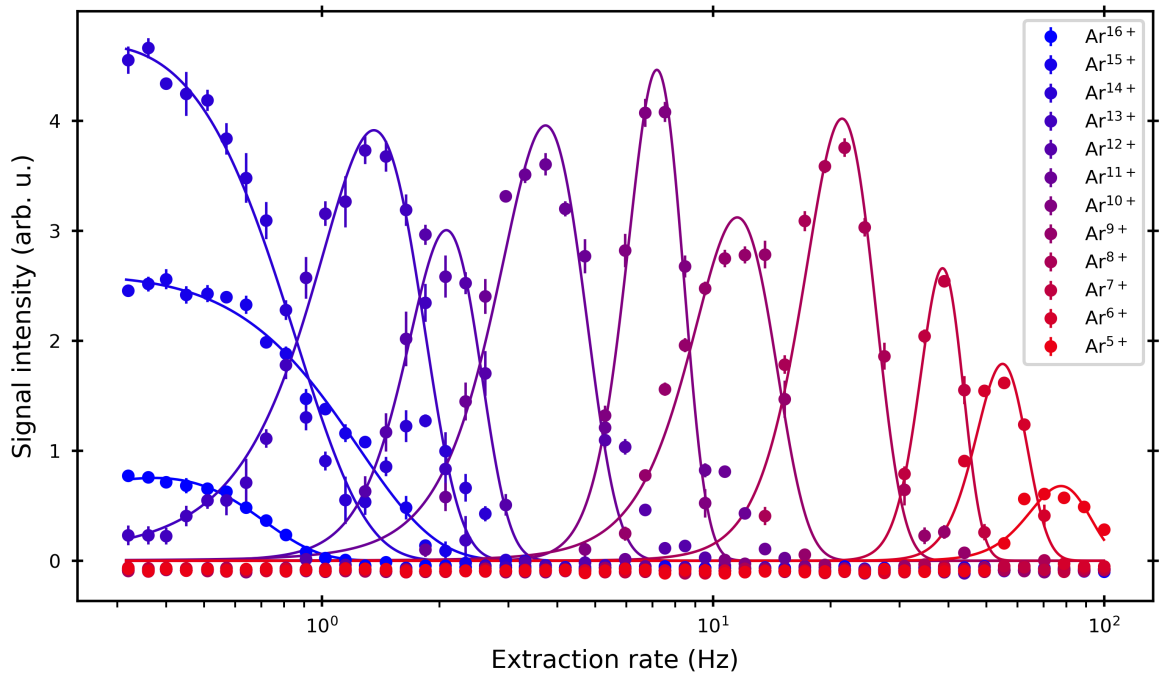

Figure 4.6: Distribution of different charge states over extraction rate. The signal is obtained by taking the signal intensity along the mean time of flight, shown in fig. 4.3. For smaller extraction times (longer breeding times), higher charge states are generated. Note that this was used as an orientation for the right extraction rate.

Timings	A	B
Time	1355.45 µs	1355.88 µs

Table 4.6: Time window chosen for the charge state selection of Ar^{14+}

found, another TOF-spectrum was recorded to show that only Ar^{14+} was selected. In fig. 4.7 also some other charge states can be seen. At higher rates, the residual gas is still visible and also a different argon charge state, leaving the selected time window at smaller extraction rates. However, choosing a smaller time window for selection lead to a smaller Ar^{14+} signal, maybe due to a long settling process of the electrode. If a small fraction of a different charge state should not be removed from the beam, later deceleration in the pulse drift tubes would generate an energy difference between these ions, rendering unwanted residuals unsuitable for retrapping.

To ensure that indeed Ar^{14+} was selected, we compared the mean time of flight of the now found signal to the time of flights predicted by the above-performed fit eq. (4.1). Comparing this to the measured time, we obtain the following time of flights listed in table 4.7.

In table 4.7 we see a significant difference for neighbouring charge states. Comparing the shape of the signal to fig. 4.3, and taking table 4.7 into account, the selected charge

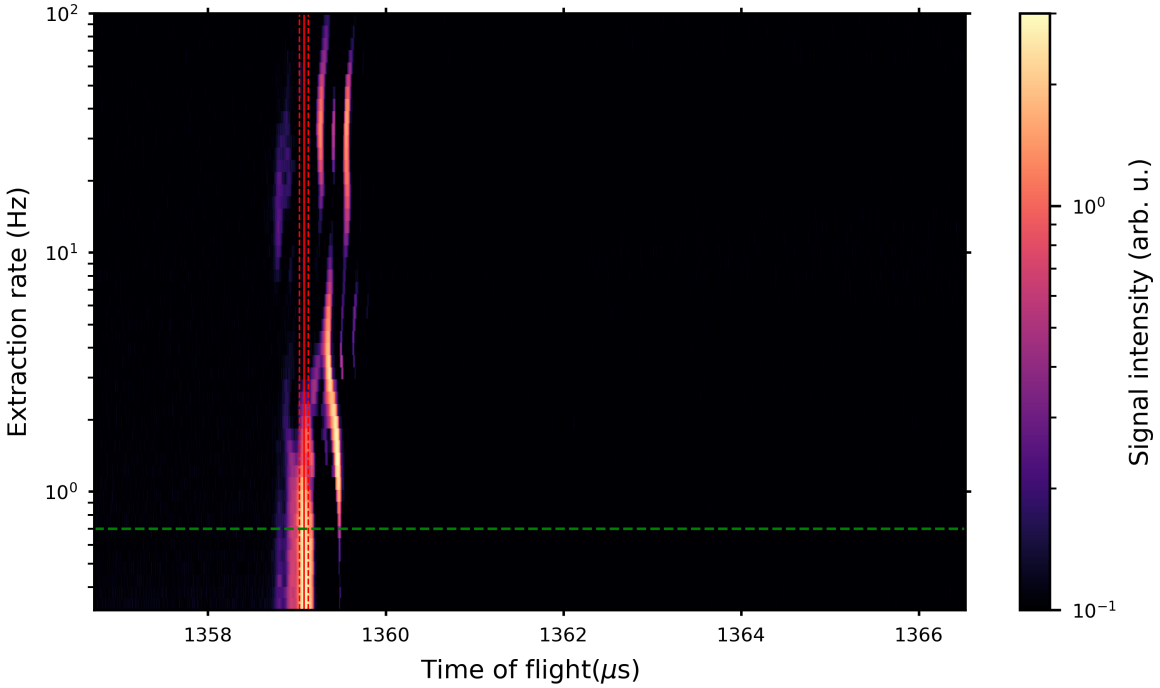

Figure 4.7: Time of flight spectra at the second MCP after selection process. A strong signal around $1359\,\mathrm{s}$ is visible. The red solid line indicates the mean time of flight, red dashed the 1σ area. At higher rates also some different charge states are visible. The green line indicates the extraction rate chosen to proceed with.

Ions	Ar^{13+}	Ar^{14+}	Ar^{15+}
Time of flight (before TOF selection)	1359.48 µs	1359.18 µs	1358.90 µs
Time of flight (measured)	1359.08(5) µs		

Table 4.7: Time of flight of some charge states obtain from the fit function compared to the time of flight of the selected charge state.

state indeed seems to be Ar^{14+}. However, the timing appears to have shifted. This could be due to the rapid switching process causing an inhomogeneity in the electrostatic potentials, or some voltage settling process still effecting the ions.

4.3 Deceleration with pulsed drift tubes

Next in the beamline, Sikler lens four (SL4) is located. SL4 is also optimized with the program described in Section 4.1, leading to the settings displayed in table 4.8.

Even though the ion bunch now only contains the selected charge state, its high kinetic energy makes it unsuitable for retrapping inside the Paul trap. To measure the energy of the ions and also the spread of the energy distribution, the retarding field analyser located at MCP2 is used. While setting the potential of the analyser to a certain value,

Electrode	SL4LO	SL4RO	SL4LU	SL4RU
Voltage	149.5 V	78.5 V	66.5 V	105.5 V

Table 4.8: Voltages applied to Sikler lens 4

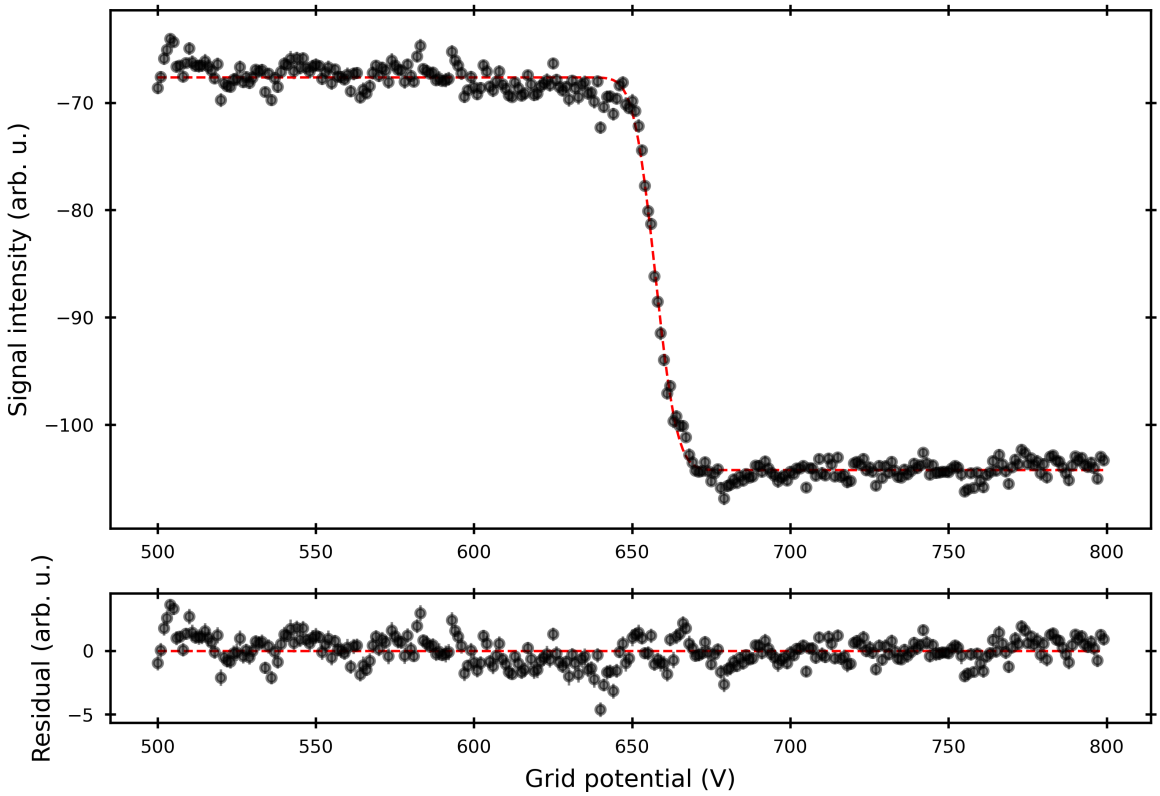

Figure 4.8: Signal intensity (black) over potential of the retarding field analyser. This allows a kinetic energy analysis of the ion beam by fitting an error function (red, dashed) to the signal.

we measure the incoming signal intensity.

Assuming a Gaussian like energy distribution of the bunch, we can fit the following function to the signal.

$$I = A\left(1 - \mathrm{erf}\left(\frac{V - V_{\mathrm{mean}}}{\sqrt{2}\sigma}\right)\right) \tag{4.2}$$

Here the intensity I is given by an amplitude A, a mean potential V_{mean} and a spread σ. From this we can extract the mean energy and the energy spread of the beam.

$$E_{\mathrm{kin}} = 657.30(14) \times q \text{ eV} \tag{4.3}$$

$$\sigma = 5.38(19) \times q \text{ eV} \tag{4.4}$$

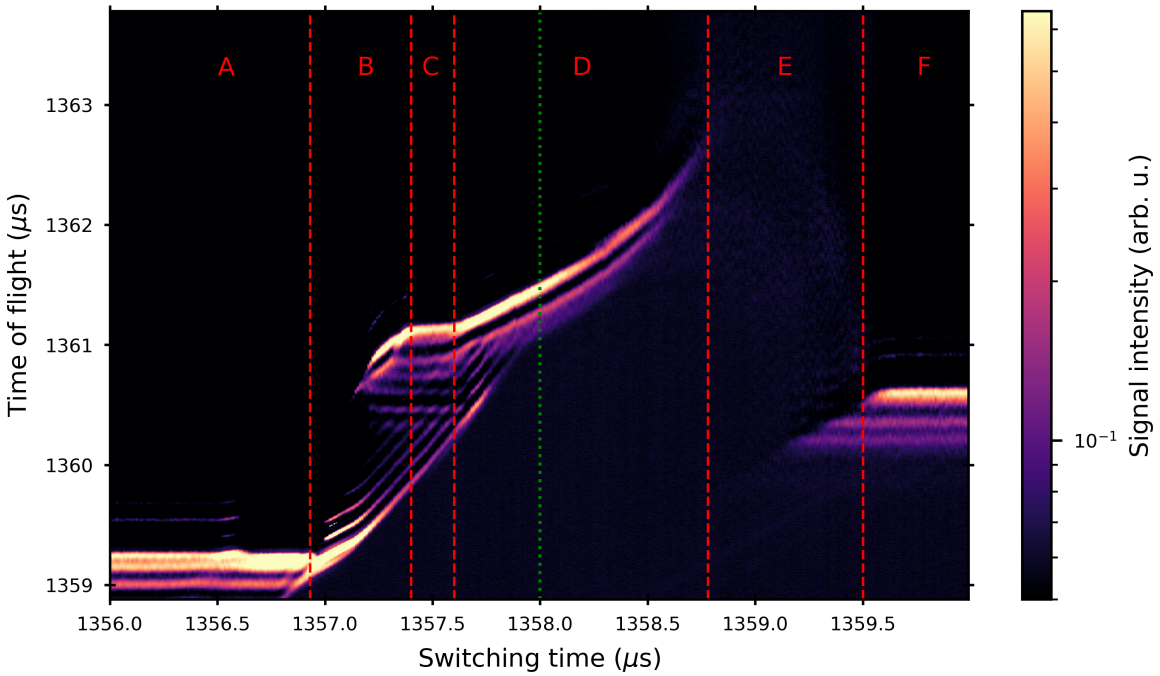

Figure 4.9: Time of flight of Ar^{14+} ions scanned over the switching time t_s of the PDTs. Different zones marked with A-F, delimited by red lines. The green line indicates the chosen timing. For details, see text.

Kinetic energies below $200 \times q$ eV can later be removed by biasing the whole Paul trap to a higher potential. However, due to technical restrictions, this is limited to 200 V. Therefore, we need to reduce the ions' energy further using the PDT with their potential explained in section 2.2.3. To obtain a kinetic energy around $100 \times q$ eV, we chose an average PDT potential $\phi_{\text{avg}} = 550\,\text{V}$. Reducing the kinetic energy by this amount should lead to the desired kinetic energy. Besides the average potential, the correct switching time t_s and the best PDT gradient needs to be determined. To find the former one, we set the PDT gradient to $\phi_{\text{diff}} = 40\,\text{V}$, corresponding to the voltages of 510 V and 690 V for the first and the second PDT electrodes respectively, and scan through the PDT timing to identify the best settings.

The time of flight spectra shown in fig. 4.9 shows different timing zones, which correspond to different positions of the ions inside the PDTs at the time of switching.

- **A:** The PDTs are pulsed down before the ions can enter the first tube. Therefore, they experience no deceleration.
- **B:** The ions enter the first electrode of the PDTs losing a significant part of their kinetic energy, recognizable by their longer time of flight.
- **C:** All ions make it inside the first electrode of the PDTs. They do not experience the potential gradient from the second electrode, yet.

- **D:** The ions enter the linearly increasing part of the potential, leading to an increased loss of kinetic energy. The ions lose energy linearly. At the end of this sector, a non-linear increase of the TOF is visible due to the $t \propto 1/\sqrt{E}$. Moreover, due to the now very slow ions, the signal gets weaker. Somewhere in this zone, the final switching time should lay to achieve the bunching effect of the PDTs.

- **E:** The signal of the ions vanishes. Somewhere at this timing, a second plateau similar to the one in section **C** is expected [30]. The lack of this is probably due to defocusing effects from the PDTs for a low energetic beam.

- **F:** The ions cross the whole PDT potential, leading to a longer TOF due to their smaller velocity inside the PDTs. Even so, the ions do not lose energy, as they regain all their kinetic energy while exiting the electrodes.

Besides already mentioned artefacts also seen in fig. 4.3, this scan shows something already mentioned in section 4.2. We see traces of at least one different charge state. Following the lines along the switching time we see in sector **B** and sector **C**, another line appears from below, indicating a different charge state. Due to their increasing time of flight, one could suggest a higher charge state, arriving at the linearly increasing potential before the desired Ar^{14+}. However, this should not be of concern, because we can choose the timing such that this signal will disappear. Additionally, an ion with a different time of flight than the intended one, for example higher charge states, will be moved further up the PDT potential and therefore not match the final deceleration step. For example, assuming the three ions Ar^{13+}, Ar^{14+} and Ar^{15+} flying with the same velocity calculated in eq. (2.22) and with the temporal spacing described in table 4.7, a spatial separation of 6 cm between Ar^{14+} and Ar^{15+} and 8 cm between Ar^{14+} and Ar^{13+} is expected. The length of the interlaced part between the electrodes is only 12 cm long. A different ion would therefore end up with a kinetic energy not matching the potential in the final step.

Based on the considerations above, we choose the PDT switching time to be

$$t_s = 1358.00\,\mu s. \tag{4.5}$$

Preceding experiments used to determine the middle of the linearly increasing potential slope, however it is not needed to match the timing with the middle of the slope to reach a deceleration. This timing was chosen, considering the decreasing signal strength for later timings. A switching prior to the middle of the mentioned potential zone will lead to a smaller energy loss, since $\phi_{avg} = 550\,V$ is not yet reached by the ions.

Now that the timing is set, we can still optimize the gradient of the PDTs to gain a smaller energy spread. Therefore, we measure the energy distribution as shown in fig. 4.8 and vary the PDT gradient.

In fig. 4.10 one can see that the width of the energy distribution slowly spreads with higher gradients. However, the normalization in this plot hides that the signal intensity also changes over the gradient. To interpret this data better, a plot, fig. 4.11, of the spread and the intensity over the gradient is made. The fraction of signal intensities per spread σ is included and taken as a figure-of-merit.

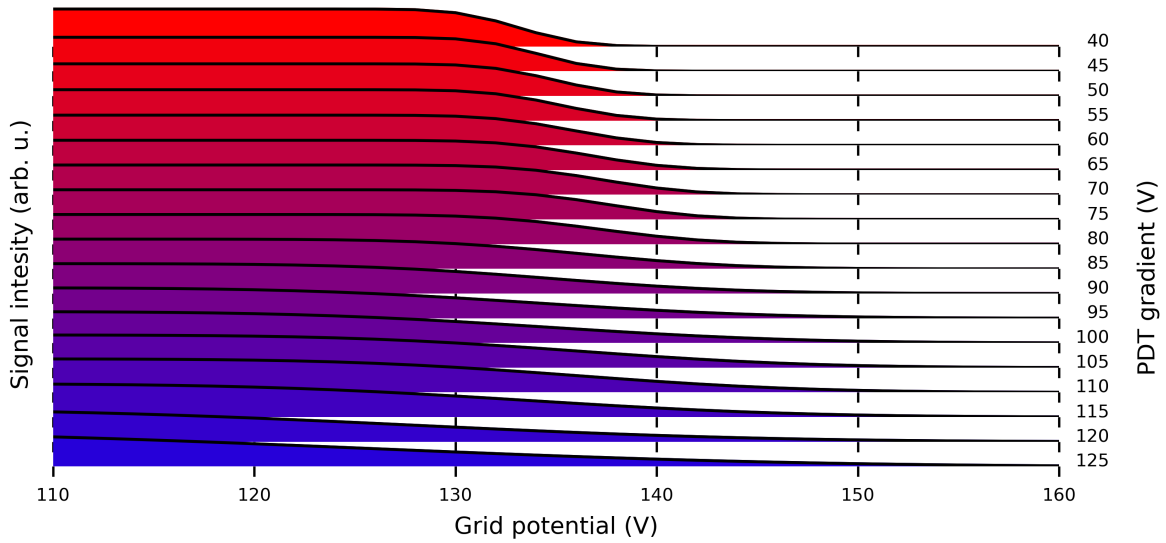

Figure 4.10: Normalized signal intensity for different retarding field analyser potentials using different PDT gradients. For larger PDT gradients, the spread visible increases.

The smallest energy spread is achieved at the smallest PDT gradient, but this comes with a rather small signal intensity. For larger gradients, a significant signal improvement could be achieved, while the energy spread nearly stayed the same. Consequently, we choose a moderate PDT gradient of 60 V to gain a strong signal while maintaining a small energy spread.

Electrodes	PDT1	PDT2
Voltages	490 V	610 V

Table 4.9: Voltages applied to the PDT electrodes to generate the wanted PDT gradient of 60 V.

Now the PDTs are fully set up to reduce the energy of the ions in the desired way. To check the ions' kinetic energy, we repeat the energy measurement from fig. 4.8.

From fig. 4.12 we obtain the following beam energy and energy spread

$$E_{\text{kin}} = 136.306(41) \times q \text{ eV} \tag{4.6}$$

$$\sigma = 3.528(57) \times q \text{ eV} \tag{4.7}$$

This energy is in the wanted order of magnitude to be slowed down by the biased potential of the Paul trap. One sees that it is slightly above the desired 100V, due to the ions not being at the centre of the PDTs but rather before the centre. However, this was expected from the chosen timing.

Optimizing the beamline with the described methods, increases signal intensity, selects

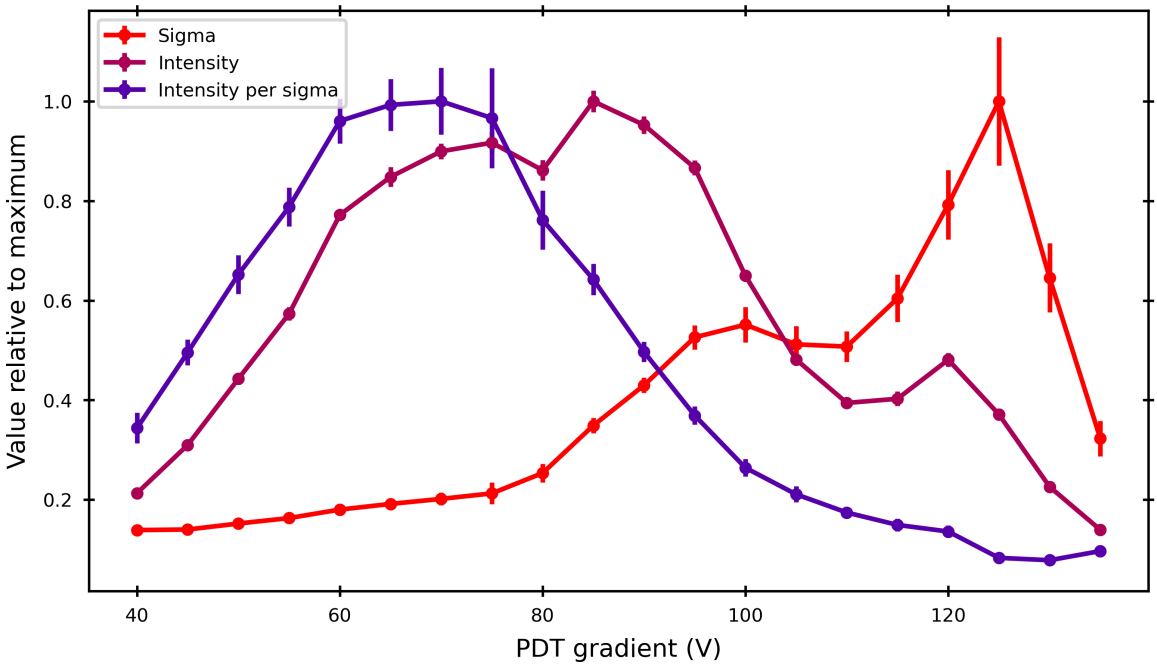

Figure 4.11: Development of energy spread sigma (red) and signal intensity (burgundy) over PDT gradients, normalized to their maximum. Also shown, the fraction of intensity per sigma (violet), indicating a optimal setting around 60 V to 75 V. The connection between the data points is purely for visualization purpose.

a particular charge state of argon, decelerates and bunches the ion beam to lead it to the Paul trap.

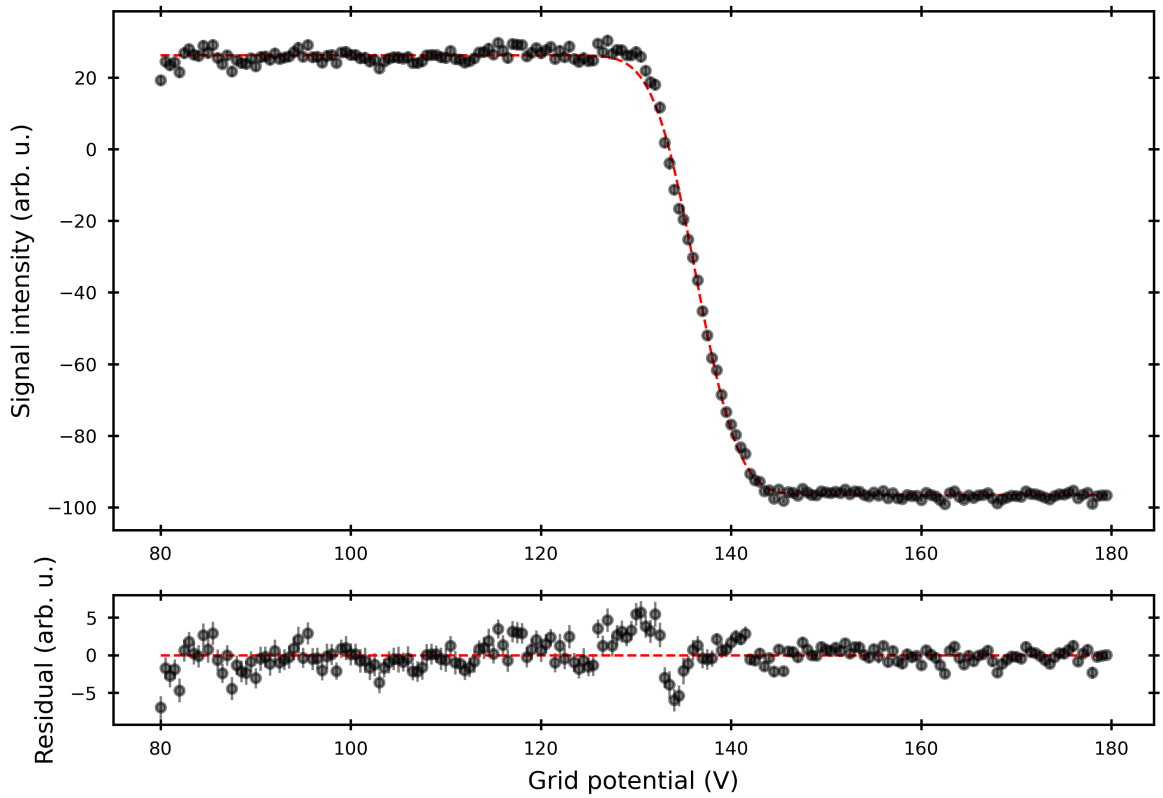

Figure 4.12: Signal intensity (black) over potential of the retarding field analyser after optimized deceleration inside the PDTs. Fitted error function (red, dashed) indicates a smaller mean energy and a smaller energy spread compared to fig. 4.8. Note the different horizontal scale.

5 Retrapping

After decelerating and bunching in the beamline, the Ar^{14+} still needs to be retrapped inside the Paul trap. Two different methods of deceleration for the residual kinetic energy are used. First, the ions are decelerated by biasing the whole trap to an elevated potential, reducing the kinetic energy. If an energy low enough is reached, the ions are then confined inside the Paul trap field radially, while being reflected back and forth between the mirror electrodes. In the final step, Ar^{14+} will be sympathetically cooled by a Be^+ crystal inside the trap, until the HCI has lost enough energy to be stopped inside the trap centre and co-crystallize with the Be^+ crystal.

5.1 Electrostatic deceleration

According to the retrapping concept explained in section 2.5 the whole trap is biased to a potential to reduce the kinetic energy of the ions further. This potential, referred to as elevated ground, should decrease the kinetic energy of the ions below or around $1 \times q$ eV. According to fig. 4.12, the mean kinetic energy is at $E_{\text{kin}} \approx 136.3 \times q$ eV. Hence, we biased the whole Paul trap to the elevated ground voltage of 136 V, hoping to maximize the number of ions with as low as possible velocity. However, this led to a complete loss of the ion's signal. While investigating the elevated ground, we observed that the acceptance of the trap got smaller and the optimal parameters for Sikler lens 5 shifted for higher elevated grounds. This needed to be taken into account. Therefore, the elevated ground was ramped up from 0 V until we saw a significant decrease in signal strength. At first, this was the case around 110 V. Now another Sikler lens optimization was done, and the elevated ground ramped up to around 125 V. From this voltage onwards, the elevated ground was ramped up in 0.5 V steps and the Sikler lens was optimized at each of these settings until we reached the desired 136 V without losing the ion signal.

Electrode	SL5LO	SL5RO	SL5LU	SL5RU
Voltage	81.25 V	79.75 V	88.75 V	82.25 V

Table 5.1: Voltages applied to Sikler lens 5.

Electrode	ELF40K	ELF4K	ELB40K	ELB4K
Voltage	98 V	98 V	92 V	0 V

Table 5.2: Voltages applied to the einzel lenses inside the thermal shields of the Paul trap.

At this step of the retrapping process, signal intensity had dropped to a low level. Approximately half, or sometimes even less, of all extracted ions led to a signal on MCP3 and these signals then also showed lower intensities. Thus, we employed the einzel lenses (EL) inside the two layers of thermal shielding of the trap to obtain better transmission. We optimized the einzel lenses in front of the Paul trap (ELF40K, ELF4K) and behind the Paul trap (ELB40K, ELB4K) until we reached better signal intensity. This was done in the same manner as the focus optimization of the Sikler lenses. However, due to a short circuit of the einzel lens in the 40 K stage behind the trap, this lens had to remain grounded the whole time.

Another way to improve the signal was by applying a stronger radial confinement potential in the Paul trap. This should also lead to a more focused ion beam. Limited by the cooling performance of the cryogenic system, currently under investigation at the experiment, the Paul trap has a maximal input power for the RF confinement. Therefore, we were limited to $-12\,\mathrm{dBm}$. Nevertheless, these two measures already allowed a significant improvement sufficient to proceed.

To verify that we are able to slow down the incoming ions, we measure their time of flight while ramping up the elevated ground.

In fig. 5.1, ions arriving later at the MCP for increasing elevated ground voltage is shown. This confirms that we are able to slow down the ions significantly. The chosen elevated ground setting seems to be reasonable, as it is just below the asymptotic limit. The longer time of flight indicates a loss of kinetic energy. Also, the decreased intensity for different elevated ground settings can be seen. The intensity drops drastically between 60 V and 110 V , caused by the setting of SL5 being suboptimal for these potentials.

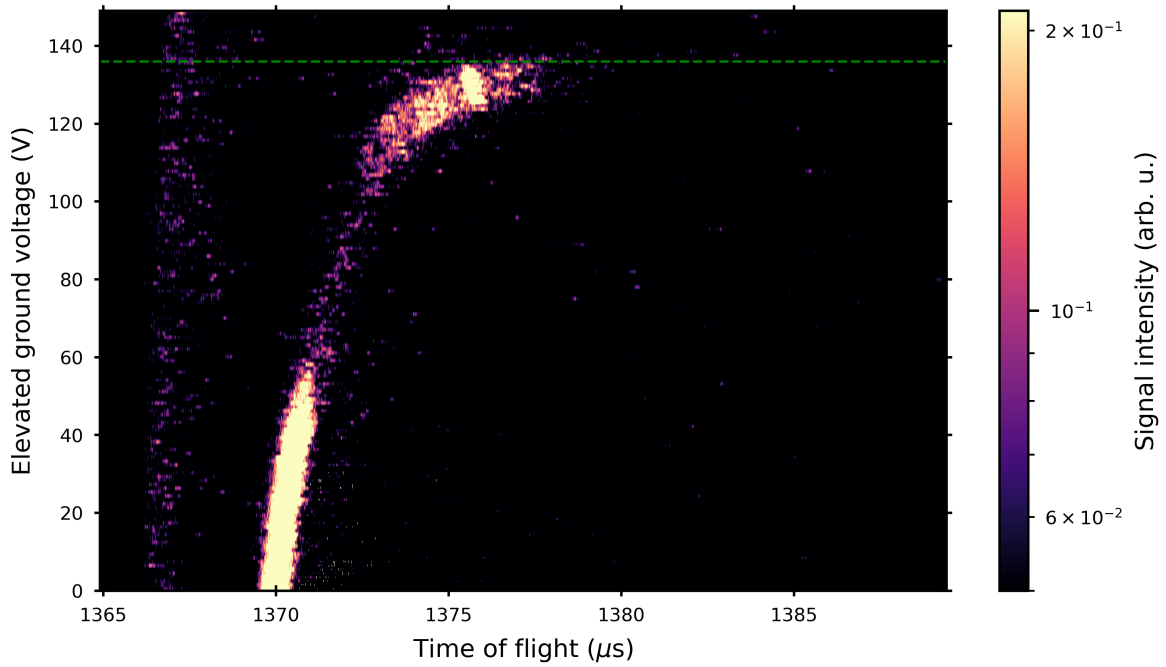

Figure 5.1: Time of flight spectra of Ar^{14+} ions for different elevated grounds, recorded with MCP3, with SL5 settings optimised for an elevated ground of 136 V. For higher elevated grounds, the ions strike the MCP at a later time, indicating a loss of kinetic energy. The signal around 1368 µs indicates that also some ions of maybe a different charge state, which are not slowed by the PDTs, end up on the MCP. An elevated ground voltage of 136 V, indicated by the green line, was the selected setting for the following steps.

5.2 Reflections inside the Paul trap

To contain the slowed ions inside the Paul trap, we now need to close the electrode mirror in front of the trap, directly after the HCIs have entered. However, here we face the difficulty of the big time constant of the mirror electrodes, already discussed in section 3.2.2. One way of still reaching a fast enough blocking of the HCIs inside the trap is to charge the mirror electrodes up over a wide voltage range, starting at a voltage slightly below the elevated ground and switching up to several hundred volts more, so the relevant voltage range around the energy of the ions is quickly overcome. On the other hand, this leads to a relatively slow opening of the mirror electrodes. This will influence the ions on the way out and may result in lower signal intensities. The opening of the mirror electrodes will not matter in the final process, which would make such effects acceptable. Therefore, we set the lower voltage of the mirror electrodes to 10 V below the elevated ground at 126 V and switch them up to 250 V, the maximal voltage provided by the used power supplies.

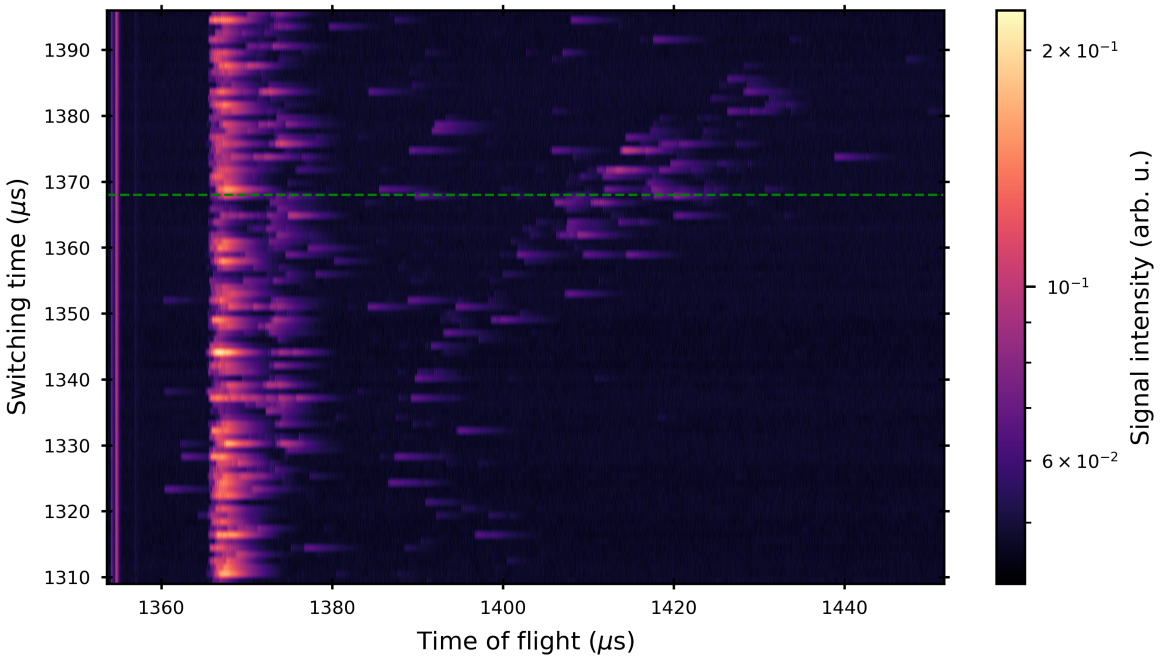

Figure 5.2: Time of flight spectrum recorded at MCP3 for varied switching of the first mirror electrode. The signal around 1368 µs is possible due to decelerated HCIs, which also can be seen in fig. 5.1. The important part is the cluster of signal around 1420 µs, indicating the measurement of reflected ions. Therefore, a switching time of 1368 µs was selected for MR1, indicated by the green line.

This being set, the correct timing of the mirror electrodes needs to be determined by the following concept. After the HCIs enter the trap MR1 needs to be closed, closing the trap behind the ions, letting them reflect several times and then opening up the second mirror to detect the signal on the MCP. Hence, we first vary the switching time of mirror electrode 2 (MR2) behind the trap, to find a timing where the ions start to be reflected at the end of the trap. MR2 gets switched between 250 V and 0 V. At the switching time 1350 µs, we saw the vanishing of the signal, indicating a reflection of the ions. However, the precise timing of this mirror electrode is not needed. In the final step, MR2 will not be switched between voltages, but will rather be set to a fixed voltage to permanently reflect the ions. Nevertheless, to investigate the right timing of MR1, the switching of MR2 is necessary.

To detect now the correct switching time of MR1, we varied the timing of this mirror between 1300 µs and 1400 µs and recorded the time of flight spectrum.

In fig. 5.2, the signal bulk around 1410 µs seems to be the first indication of ions being reflected back and forth in the trap, compared to the time of flight seen in fig. 5.1. Comparing these two images, the enormously decreased signal intensity can be seen, comparing the intensity of the signal around 1398 µs. Therefore, we set the switching time of MR1 to 1368 µs

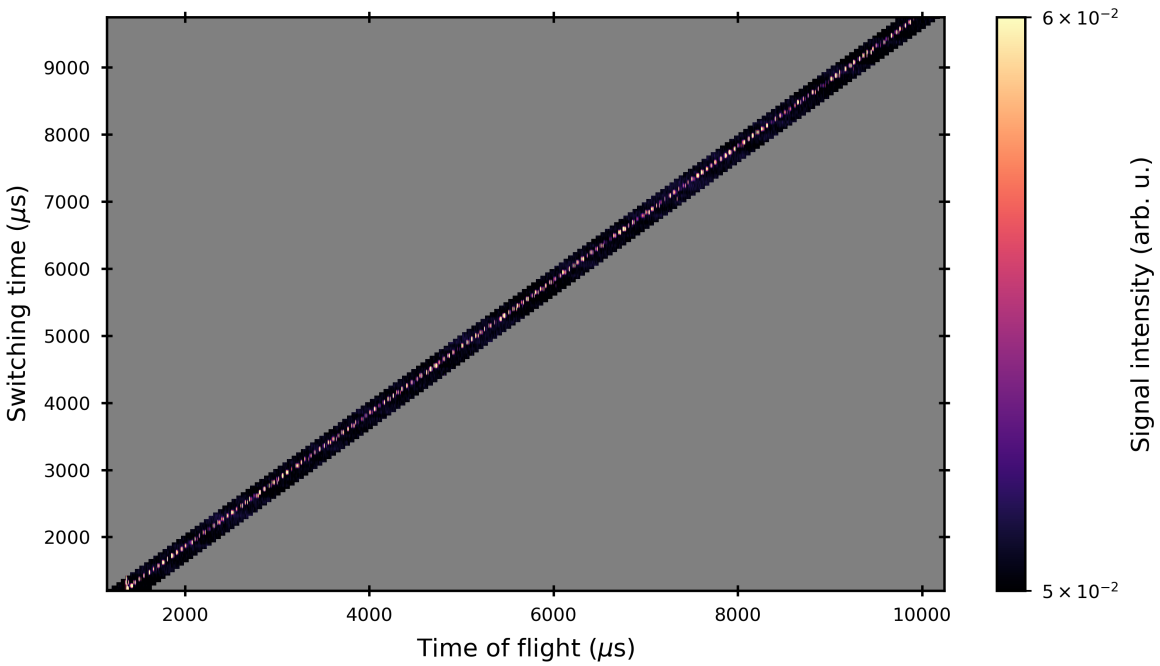

Figure 5.3: Time of flight spectra measured at MCP3 for different switching times of the second mirror electrode. For each line, the switching and the oscilloscope scope was moved $50\,\mu s$ later. The signal (yellow) of reflected ions arrives later for later switching of MR2. Only the black corridor was measured, the grey surrounding was not measured. The scope of the oscilloscope had to be moved with the switching due to resolution constraints. This demonstrated multiple reflections of the HCIs and confinement times up to $9\,ms$

However, to achieve a co-crystallisation of the HCI inside the Be^+ crystal, the ions need to be reflected thousands of times [44]. This corresponds to a storage time above the millisecond range. To evaluate the signal loss for more reflections than just back and forth once like in fig. 5.2, we delay the switching of MR2 to achieve more reflections inside the Paul trap. As we can see here in fig. 5.3, we were able to receive a signal of stored ions even after around 9 ms. To confirm that this signal is indeed a reflected HCI and, e.g., not just a crosstalk from the switching process, we evaluate the signal with individual critical functions turned off deliberately. First, we just turn off the switching of both mirror electrodes. Then we turn off the injection of argon into the EBIT by closing the needle valve of the injection system. Finally, we turn off the radial trapping potential of the Paul trap. Only when all systems are turned on, we receive the signal.

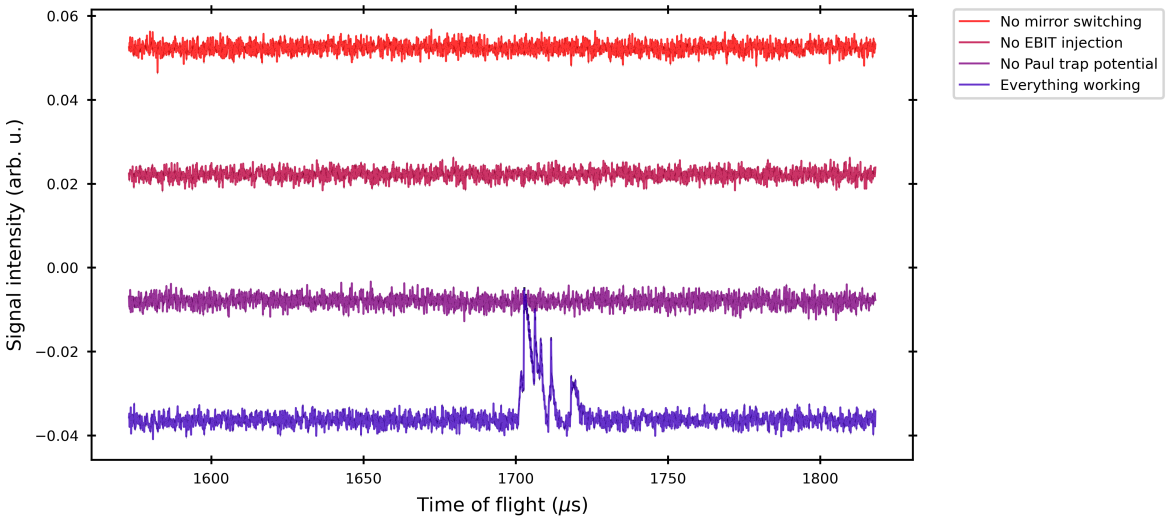

Figure 5.4: Signal at MCP3 for a Time of flight only reachable with multiple reflections inside the trap. For each trace, one single necessary mechanism was turned off. From top to bottom: No trigger signal for mirror switching, no neutral gas injection of argon into the EBIT, no RF quadrupole field inside the Paul trap, and every component working as intended. Note that all other mechanisms were operating if not mentioned otherwise. This verifies that the signal was indeed coming from reflected HCIs.

5.3 Co-crystallization

From these promising results, we moved on to the final step of the retrapping scheme. A Be^+ crystal is needed inside the Paul trap to cool the HCIs sympathetically section 2.4.2. Therefore, Be^+ ions need to be loaded into the trap. They are produced directly inside the trap centre by overlapping a collimated beryllium atom beam from the atomic oven setup with a photoionization laser like described in section 3.2.3. This laser operates at 235 nm and ionizes beryllium atoms via a two-photon process. Afterwards, these ions are laser cooled to create a cold Coulomb crystal inside the trap centre, axially confined by a potential of 0.875 V. However, we found that the Be^+ ions were affected by the required switching of the mirror electrodes. During the attempts of retrapping we saw that all Be^+ ions were ejected from the Paul trap as soon as the mirror electrodes were turned on. It was found that this effect depends on the voltage range over which the mirror electrodes were switched. At small voltage differences of up to 30 V, the crystal remained stable inside the Paul trap, but at larger differences, all ions were lost. To investigate this issue, the cables connected to several electrodes were monitored with an oscilloscope while switching the mirror electrode, revealing significant crosstalk between several electrodes and both mirror electrode. A transient voltage on one trap electrode could also explain the loss of the ions, by kicking them out of the trap potential. A connector box bundling the signals for the different electrodes into a single cable was identified as a potential

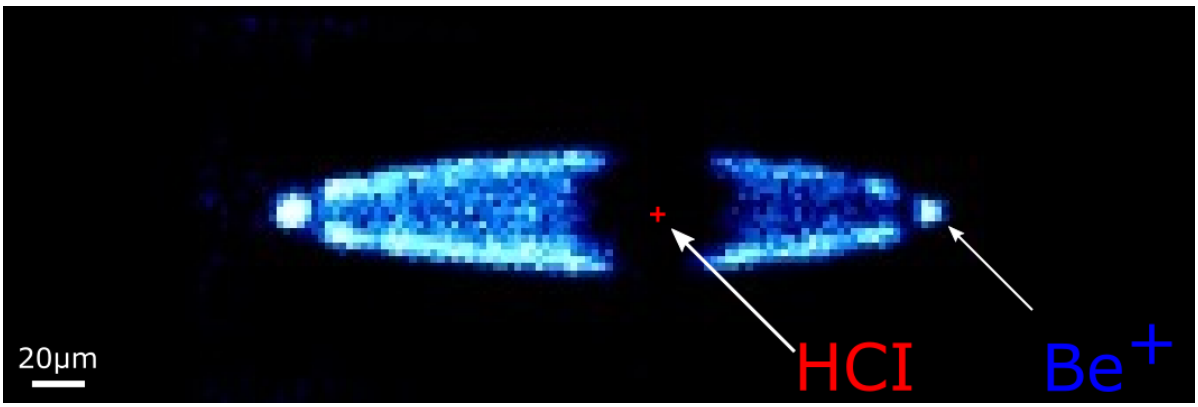

Figure 5.5: Image of the first HCI sitting inside a partially crystallized Be^+ crystal inside the Paul trap. Through their higher charge, HCIs repel single charge ions more and therefore occupy more space inside the crystal. The HCI does not interact with the cooling laser, presenting itself as a black spot inside the fluorescent crystal.

source of the crosstalk. However, even setting up a new cable, allowing a separated port for the mirror electrodes, showed no significant improvement, indicating that most of the pick-up happened inside the vacuum system, making a reduction more difficult. Further investment in the stability of the ions showed that the wavelength of the cooling laser plays a major role in the stability of the Coulomb crystal, during the switching of the mirror electrodes. If the wavelength of the cooling laser was detuned by about 200 MHz, the ions withstood the switching process up to a voltage difference of 54 V. Therefore, we choose a new upper limit of switching for the first mirror electrode of 180 V. One downside of this was the loss of imaging quality. The Be^+ ions were no longer spatially distinguishable due to a lower fluorescence. Only the presence of the crystal inside the trap was still detectable. Finally, the second mirror electrode was set to a constant value of 180 V.

With this all set up, the switching of the first mirror electrode was activated with the above described detuning. After a few minutes, the switching was turned off and the laser was tuned closer to the resonance frequency, cooling the crystal to lower temperatures and making the individual ions distinguishable again. This revealed that the first highly charged ion was trapped inside the Paul trap.

Further investigation following this procedure showed a consistent ability to load HCIs inside the trap with just a loading time of a few minutes, sometimes even showing multiple HCIs trapped at once. By tuning the laser wavelength closer to the Be^+ laser cooling transition, a cold mixed crystal could be obtained, showing promising results for the next steps of the experiment. The loaded HCIs showed already a promising stability, lasting over ten minutes inside the trap, until being ejected due to charge exchange with residual gas.

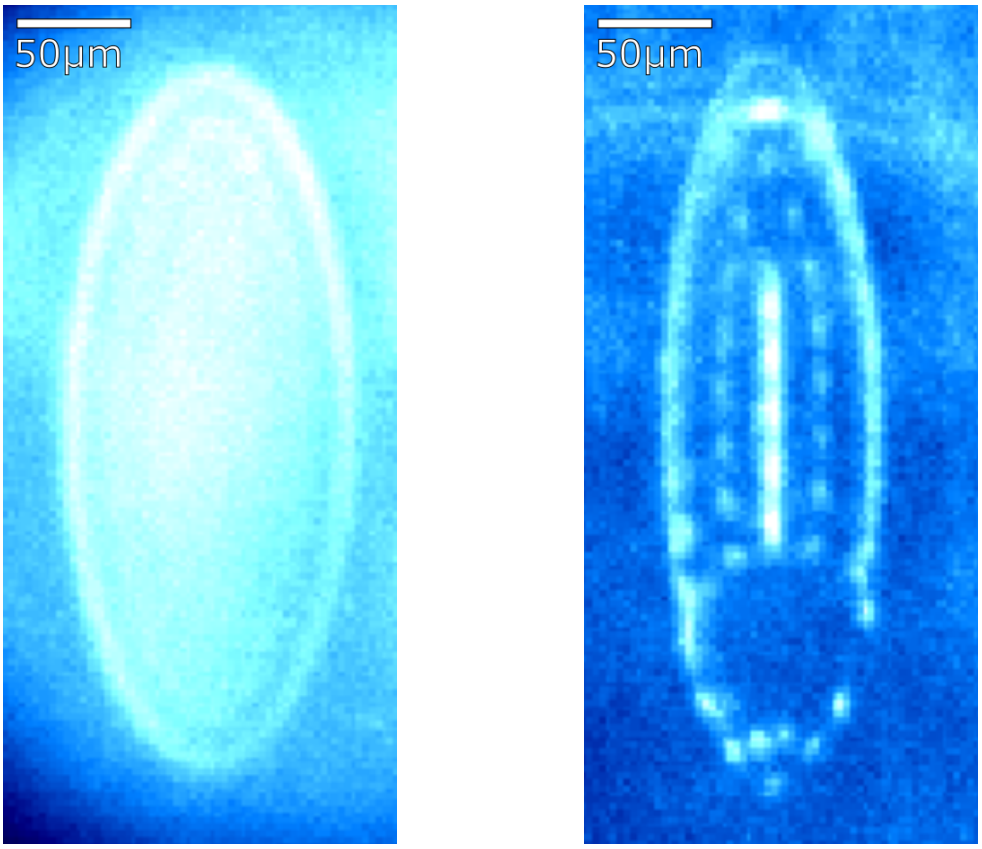

(a) (b)

Figure 5.6: **(a)** Large Be^+ ensemble inside the trap, suitable for the cooling of injected HCIs. One can see, that the ions a partially spatial ordered. Single ions are not observable. **(b)** HCI embedded into a Be^+ crystal. The crystal is recognizably colder than in (a), since single ions can be distinguished. The HCI does not interact with the cooling laser, therefore leaving a darker spot in the crystal.

6 Summary and Outlook

The aim of this thesis was, to trap the first highly charged ions inside the Paul trap of CryPTEx II. Argon ions were produced inside an EBIT by injecting a neutral gas jet into the trap. By extracting the ions into a beamline, the ions were guided towards the cryogenic Paul trap. An optimization algorithm was implemented to maximize the signal yield and applied to the Sikler lenses along the flight path of the ions. At an MCP detector, the different charge states inside the ion beam could be resolved, making use of their different time of flight for different charge states. This showed that a broad range of charge states of argon could be produced. These charge states then were distinguished and identified by the temporal spacing between their time of flight, leading to the identification of Ar^{5+} up to Ar^{16+}. Afterwards, one charge state was selected, Ar^{14+} , by pulsing of an electrode along the beamline. A measurement of the kinetic energy of these Ar^{14+} ions showed a Gaussian like energy distribution with 657.30(14) $\times q$ eV mean kinetic energy and a spread of 5.38(19) $\times q$ eV. This was reduced inside pulsed drift tubes. After examining the correct switching time and optimising the gradient of the system for a low energy spread and a high signal yield, a kinetic energy of 136.306(41) $\times q$ eV with an energy spread of 3.528(57) $\times q$ eV was achieved. Now these slow ions were injected into the cryogenic Paul trap. By biasing the whole trap to a potential around the kinetic energy of the ions, their velocity was further reduced. After examining the correct timing for lowering the potential of the first mirror electrode to allow a bunch of HCIs to enter the trap, reflection of HCIs along the trap axis could be observed for up to 9 µs. This promised a successful co-crystallization of the HCIs. After adjustments to the laser cooling system and the mirror electrode switching process due to issues between the switching and ion stability inside the trap, the first HCI co-crystallised with Be+ ions in the Paul trap. In the end, the system showed a consistent loading process, taking about a minute to load a highly charged ion.

Simultaneous to the end of this work, already some improvements are commissioned to improve issues identified during this work. Changes were made to the laser setup to provide two cooling lasers, one of which is permanently detuned to observe the process of capturing the HCI. Also, a new design study for the mirror electrodes is being done at the moment, trying to shield the mirror electrodes from the RF field, thereby making a large resistance currently installed in the connections to the mirror electrodes no longer necessary, allowing much smaller time constants and thus a much faster switching of the electrodes.

In the end, the methods presented in this work offer a general approach for the retrapping of highly charged ions, not limited to just Ar^{14+} . A change of the selected charge state should quickly be possible, and even the exchange of the element should easily be possible with just minor changes to the EBIT and the beamline.

This work forms a crucial step for the CryPTEx II experiment towards its scientific goal of high precision spectroscopy of highly charged ions. It immediately enables studying the dynamics of the produced mixed species ion crystals, including how the crystal configuration and stability depend on the charge to mass ratios of the constituent ions. In the near future, a new laser system will be employed to reduce the temperature of the trapped ions further. The system will cool the ions by resolved sideband cooling to allow quantum logic spectroscopy of HCIs. Even further steps include the use of an XUV frequency comb to do direct frequency comb spectroscopy of highly charged ions. Overall, this offers the possibility to test α for variations in the proposed range.

Other applications besides fundamental research are conceivable for these ultra cold HCIs. The VAUQSI experiment, started last autumn, aims to employ a comparable setup in order to employ these HCIs as ultra stable qubits to build a quantum computer inside the Paul trap with long coherence times. Both concepts are exciting new approaches for different goals, relying on the extraordinary characteristics featured by HCIs.

Bibliography

[1] K.A. Olive. "Review of Particle Physics". In: *Chinese Physics C* 40.10 (Oct. 2016), p. 100001. DOI: 10.1088/1674-1137/40/10/100001. URL: https://doi.org/10.1088/1674-1137/40/10/100001.

[2] A. Kusenko M. Dine. "Of the matter-antimatter asymmetry". In: *Rev. Mod. Phys.* 76 (1 Dec. 2003), pp. 1–30. DOI: 10.1103/RevModPhys.76.1. URL: https://link.aps.org/doi/10.1103/RevModPhys.76.1.

[3] S. Perlmutter. "Nobel Lecture: Measuring the acceleration of the cosmic expansion using supernovae". In: *Rev. Mod. Phys.* 84 (3 Aug. 2012), pp. 1127–1149. DOI: 10.1103/RevModPhys.84.1127. URL: https://link.aps.org/doi/10.1103/RevModPhys.84.1127.

[4] C. S. Wood et al. "Measurement of Parity Nonconservation and an Anapole Moment in Cesium". In: *Science* 275.5307 (1997), pp. 1759–1763. DOI: 10.1126/science.275.5307.1759.

[5] Jean-Philippe Uzan. "Varying Constants, Gravitation and Cosmology". In: *Living Reviews in Relativity* 14.1 (Mar. 2011). ISSN: 1433-8351. DOI: 10.12942/lrr-2011-2. URL: http://dx.doi.org/10.12942/lrr-2011-2.

[6] Michael T. Murphy et al. "Constraining Variationsin the Fine-Structure Constant, Quark Massesand the Strong Interaction". In: *Astrophysics, Clocks and Fundamental Constants*. Ed. by Savely G. Karshenboim and Ekkehard Peik. Berlin, Heidelberg: Springer Berlin Heidelberg, 2004, pp. 131–150. ISBN: 978-3-540-40991-5. DOI: 10.1007/978-3-540-40991-5_9. URL: https://doi.org/10.1007/978-3-540-40991-5_9.

[7] G. Kirchhoff and R. Bunsen. "Chemische Analyse durch Spectralbeobachtungen". In: *Annalen der Physik* 189.7 (1861), pp. 337–381. URL: https://onlinelibrary.wiley.com/doi/abs/10.1002/andp.18611890702.

[8] A. Bauch, P. Hetzel, and Dirk Piester. "Zeit- und Frequenzverbreitung mit DCF77: 1959-2009 und darüber hinaus". In: *PTB Mitteilungen: Amts - und Mitteilungsblatt der Physikalisch - Technischen Bundesanstalt Braunschweig - Berlin* 119 (Jan. 2009), pp. 217–240.

[9] W. Paul. "Electromagnetic traps for charged and neutral particles". In: *Rev. Mod. Phys.* 62 (3 June 1990), pp. 531–540. DOI: 10.1103/RevModPhys.62.531. URL: https://link.aps.org/doi/10.1103/RevModPhys.62.531.

[10] B. J. Bloom et al. "An optical lattice clock with accuracy and stability at the 10-18 level". In: *Nature* 506.7486 (Jan. 2014), pp. 71–75. DOI: 10.1038/nature12941.

[11] V. A. Dzuba, V. V. Flambaum, and M. V. Marchenko. "Relativistic effects in Sr, Dy, Yb II, and Yb III and search for variation of the fine-structure constant". In: *Phys. Rev. A* 68 (2 Aug. 2003), p. 022506. DOI: 10.1103/PhysRevA.68.022506. URL: https://link.aps.org/doi/10.1103/PhysRevA.68.022506.

[12] M.G. Kozlov et al. "Search for new physics with atoms and molecules". In: *Rev. Mod. Phys.* 90 (2 June 2018), p. 025008. DOI: 10.1103/RevModPhys.90.025008.

[13] M. Aschwanden. *Physics of the Solar Corona*. Springer-Verlag GmbH, Aug. 2006. 908 pp. ISBN: 9783540307662. URL: https://www.ebook.de/de/product/11430811/markus_aschwanden_physics_of_the_solar_corona.html.

[14] G. W. Series T. W. Hänsch A. L. Schawlow. "The Spectrum of Atomic Hydrogen". In: *Scientific American* 240.3 (Mar. 1979), pp. 94–111. DOI: 10.1038/scientificamerican0379-94.

[15] L. Schmöger et al. "Coulomb crystallization of highly charged ions". In: *Science* 347.6227 (2015), pp. 1233–1236. DOI: 10.1126/science.aaa2960. URL: https://www.science.org/doi/abs/10.1126/science.aaa2960.

[16] P. O. Schmidt et al. "Spectroscopy Using Quantum Logic". In: *Science* 309.5735 (July 2005), pp. 749–752. DOI: 10.1126/science.1114375.

[17] Steven A. King et al. "Algorithmic Ground-State Cooling of Weakly Coupled Oscillators Using Quantum Logic". In: *Phys. Rev. X* 11 (4 Dec. 2021), p. 041049. DOI: 10.1103/PhysRevX.11.041049. URL: https://link.aps.org/doi/10.1103/PhysRevX.11.041049.

[18] J. Stark et al. "An ultralow-noise superconducting radio-frequency ion trap for frequency metrology with highly charged ions". In: *Review of Scientific Instruments* 92.8 (2021), p. 083203. DOI: 10.1063/5.0046569.

[19] J. Nauta et al. "XUV frequency comb production with an astigmatism-compensated enhancement cavity". In: *Opt. Express* 29.2 (Jan. 2021), pp. 2624–2636. DOI: 10.1364/OE.414987. URL: http://opg.optica.org/oe/abstract.cfm?URI=oe-29-2-2624.

[20] M. A. Levine et al. "The Electron Beam Ion Trap: A New Instrument for Atomic Physics Measurements". In: *Physica Scripta* T22 (Jan. 1988), pp. 157–163. DOI: 10.1088/0031-8949/1988/t22/024.

[21] P. Micke et al. "The Heidelberg compact electron beam ion traps". In: *Review of Scientific Instruments* 89.6 (2018), p. 063109. DOI: 10.1063/1.5026961.

[22] S. Earnshaw. "On the Nature of the Molecular Forces which regulate the Constitution of the Luminiferous Ether". In: *Trans. Camb. Phil. Soc.* 7 (1842), pp. 97–112.

[23] C. Schweiger. "Construction and commissioning of a room-temperature electron beam ion trap and development of a wire probe injection system". MA thesis. Ruprecht-Karls-Universität Heidelberg, 2017. URL: http://hdl.handle.net/21.11116/0000-0005-5B37-8.

[24] J.D. Gillapsy. *Trapping highly charged ions: Fundamentals and Applications*. Huntington, N.Y: Nova Sciene Publishers, Inc., 2001. ISBN: 156072-725-X.

[25] B. M. Penetrante et al. "Evolution of ion-charge-state distributions in an electron-beam ion trap". In: *Phys. Rev. A* 43 (9 May 1991), pp. 4861–4872. DOI: 10.1103/PhysRevA.43.4861. URL: https://link.aps.org/doi/10.1103/PhysRevA.43.4861.

[26] J. R. Crespo López-Urrutia and Z. Harman. "Emission and Laser Spectroscopy of Trapped Highly Charged Ions in Electron Beam Ion Traps". In: *Fundamental Physics in Particle Traps*. Ed. by Wolfgang Quint and Manuel Vogel. Berlin, Heidelberg: Springer Berlin Heidelberg, 2014, pp. 315–373. ISBN: 978-3-642-45201-7. DOI: 10.1007/978-3-642-45201-7_10.

[27] W. Lotz. "Electron-impact ionization cross-sections and ionization rate coefficients for atoms and ions from hydrogen to calcium". In: *Zeitschrift für Physik* 216.3 (June 1968), pp. 241–247. DOI: 10.1007/bf01392963.

[28] Y. S. Kim and R. H Pratt. "Direct radiative recombination of electrons with atomic ions: Cross sections and rate coefficients". In: *Phys. Rev. A* 27 (6 June 1983), pp. 2913–2924. DOI: 10.1103/PhysRevA.27.2913.

[29] A. Müller and E. Salzborn. "Scaling of cross sections for multiple electron transfer to highly charged ions colliding with atoms and molecules". In: *Physics Letters A* 62.6 (1977), pp. 391–394. ISSN: 0375-9601. DOI: https://doi.org/10.1016/0375-9601(77)90672-7.

[30] M. K. Rosner. "Production and preparation of highly charged ions for re-trapping in ultra-cold environments". MA thesis. Ruprecht-Karls-Universität, Heidelberg, 2019. URL: http://hdl.handle.net/21.11116/0000-0005-5B37-8.

[31] R.E. Marrs. "Self-cooling of highly charged ions during extraction from electron beam ion sources and traps". In: *Nuclear Instruments and Methods in Physics Research Section B: Beam Interactions with Materials and Atoms* 149.1 (1999), pp. 182–194. ISSN: 0168-583X. DOI: https://doi.org/10.1016/S0168-583X(98)00624-7.

[32] L. Schmoeger. "Ein elektrodynmaisches System für den Transfer hochgeladener Ionen in eine Paulfalle". MA thesis. Ruprecht-Karls-Universität Heidelberg, 2013. URL: http://hdl.handle.net/11858/00-001M-0000-000E-EDFE-0.

[33] H. Rose. *Geometrical charged-particle optics*. Berlin: Springer, 2009. ISBN: 9783540859154.

[34] H. Liebl. *Applied Charged Particle Optics*. Springer, 2008. ISBN: 978-3-540-71925-0. DOI: 10.1007/978-3-540-71925-0.

[35] F. Hinterberger. "Ion optics with electrostatic lenses". en. In: (2006). DOI: 10.5170/CERN-2006-012.27.

[36] J. D. Jackson. *Klassische Elektrodynamik*. De Gruyter, 2013. ISBN: 9783110334470. DOI: doi:10.1515/9783110334470.

[37] H. Kreckel et al. "A simple double-focusing electrostatic ion beam deflector". In: *Review of Scientific Instruments* 81.6 (2010), p. 063304. DOI: 10.1063/1.3433485.

[38] J. Stark. "Design ultrastabiler Hochfrequenzfelderfür die Langzeitspeicherunghochgeladener Ionen". MA thesis. Ruprecht-Karls-Universität Heidelberg, 2015. URL: http://hdl.handle.net/11858/00-001M-0000-0027-7984-C.

[39] J. Stark. "An Ultralow-Noise Superconducting Radio-Frequency Ion Trap for Frequency Metrology with Highly Charged Ions". PhD thesis. Ruprecht-Karls-Universität Heidelberg, 2020. URL: http://hdl.handle.net/21.11116/0000-0007-67D1-9.

[40] D. Leibfried et al. "Quantum dynamics of single trapped ions". In: *Rev. Mod. Phys.* 75 (1 Mar. 2003), pp. 281–324. DOI: 10.1103/RevModPhys.75.281. URL: https://link.aps.org/doi/10.1103/RevModPhys.75.281.

[41] D. J. Larson et al. "Sympathetic cooling of trapped ions: A laser-cooled two-species nonneutral ion plasma". In: *Phys. Rev. Lett.* 57 (1 June 1986), pp. 70–73. DOI: 10.1103/PhysRevLett.57.70.

[42] L. Schmöger et al. "Deceleration, precooling, and multi-pass stopping of highly charged ions in Be+ Coulomb crystals". In: *Review of Scientific Instruments* 86.10 (2015), p. 103111. DOI: 10.1063/1.4934245.

[43] M. Drewsen. "Ion Coulomb crystals". In: *Physica B: Condensed Matter* 460 (2015). Special Issue on Electronic Crystals (ECRYS-2014), pp. 105–113. ISSN: 0921-4526. DOI: https://doi.org/10.1016/j.physb.2014.11.050. URL: https://www.sciencedirect.com/science/article/pii/S0921452614008849.

[44] L. Schmöger. "Kalte hochgeladene Ionen für Frequenzmetrologie". PhD thesis. Ruprecht-Karls-Universität Heidelberg, 2017. URL: http://hdl.handle.net/11858/00-001M-0000-002E-25A5-B.

[45] P. Micke. "Quantum Logic Spectroscopy of Highly Charged Ions". en. PhD thesis. Gottfried Wilhelm Leibniz Universität Hannover und Physikalisch-Technische Bundesanstalt, 2020. DOI: 10.7795/110.20201222.

[46] G. Sikler P. Mandal and M. Mukherjee. "An einzel lens with a diagonal-slit central electrode to combine steering and focusing of a low energy ion beam". In: *JINST 1106:02004,2011* (July 2010). DOI: 10.1088/1748-0221/6/02/P02004. arXiv: 1007.1592 [nucl-ex].

[47] J. Ladislas Wiza. "Microchannel plate detectors". In: *Nuclear Instruments and Methods* 162.1 (1979), pp. 587–601. ISSN: 0029-554X. DOI: https://doi.org/10.1016/0029-554X(79)90734-1.

[48] P. Micke et al. "Closed-cycle, low-vibration 4 K cryostat for ion traps and other applications". In: *Review of Scientific Instruments* 90.6 (2019), p. 065104. DOI: 10.1063/1.5088593.

[49] Hermann Hinsch. *Elektronik*. Springer-Verlag GmbH, Mar. 2013. 292 pp. ISBN: 9783642614699. URL: https://www.ebook.de/de/product/33494843/hermann_hinsch_elektronik.html.

[50] A. Garmendia Navarro. *Towards re-trapping highly charged argon in a cryogenic Paul trap experiment*. 2021.

[51] C. Warnecke. "Imaging of Coulomb crystals in a cryogenic Paul trap experiment". MA thesis. Ruprecht-Karls-Universität Heidelberg, 2019. URL: http://hdl.handle.net/21.11116/0000-0004-F47D-D.

[52] A. Kramida et al. NIST Atomic Spectra Database (ver. 5.9), [Online]. Available: https://physics.nist.gov/asd [2021, December 20]. National Institute of Standards and Technology, Gaithersburg, MD. 2021.

Acknowledgments

In the end, I would like to thank all people who helped and supported me in the preparation of this Bachelor thesis and mention some significant people here explicitly. First, I would like to thank Prof. Dr. José Ramón Crespo López-Urrutia for letting me conduct my thesis at such an interesting experiment. Also, I would like to thank Malte Wehrheim, who took significant part in the whole process, especially in figuring out how to deal with the beamline. Besides that I also want to thank him and Claudia Volk, Christian Warnecke, Alvaro Garmendia and Elwin Dijck for proofreading this work several times. Also, many thanks to the rest of the CryPTEx-II team. Additionally, I want to thank the all people of the Studentenbüro for helpful tips, advices and a funny time at the MPIK.

Last but not least I want to thank, Paula, Philipp, Amelie, Daniel, Ida, Michael, and Ortrud for their support through stressful times.

Erklärung

Ich versichere, dass ich diese Arbeit selbstständig verfasst und keine anderen als die angegebenen Quellen und Hilfsmittel benutzt habe.

Heidelberg, den 30.01.2022,